**Biophysical** Journal

**Article** 



# An ensemble of cadherin-catenin-vinculin complex employs vinculin as the major F-actin binding mode

Bright Shi, 1,2 Tsutomu Matsui, 3 Shuo Qian, 4 Thomas M. Weiss, 3 Iain D. Nicholl, 5 David J. E. Callaway, 1,\* and Zimei Bu1,2,\*

<sup>1</sup>Department of Chemistry and Biochemistry, City College of New York, City University of New York (CUNY), New York; <sup>2</sup>PhD Programs in Chemistry and Biochemistry, CUNY Graduate Center, New York; <sup>3</sup>Stanford Synchrotron Radiation Light Source, Menlo Park, California; <sup>4</sup>Second Target Station Project, Oak Ridge National Laboratory, Oak Ridge, Tennessee; and <sup>5</sup>Department of Biomedical Science and Physiology, Faculty of Science and Engineering, University of Wolverhampton, Wolverhampton, United Kingdom

ABSTRACT The cell-cell adhesion cadherin-catenin complexes recruit vinculin to the adherens junction (AJ) to modulate the mechanical couplings between neighboring cells. However, it is unclear how vinculin influences the AJ structure and function. Here, we identified two patches of salt bridges that lock vinculin in the head-tail autoinhibited conformation and reconstituted the full-length vinculin activation mimetics bound to the cadherin-catenin complex. The cadherin-catenin-vinculin complex contains multiple disordered linkers and is highly dynamic, which poses a challenge for structural studies. We determined the ensemble conformation of this complex using small-angle x-ray and selective deuteration/contrast variation small-angle neutron scattering. In the complex, both α-catenin and vinculin adopt an ensemble of flexible conformations, but vinculin has fully open conformations with the vinculin head and actin-binding tail domains well separated from each other. F-actin binding experiments show that the cadherin-catenin-vinculin complex binds and bundles F-actin. However, when the vinculin actin-binding domain is removed from the complex, only a minor fraction of the complex binds to F-actin. The results show that the dynamic cadherin-cateninvinculin complex employs vinculin as the primary F-actin binding mode to strengthen AJ-cytoskeleton interactions.

SIGNIFICANCE The adherens junctions (AJs) are multiprotein complexes that sense and transduce cellular mechanical forces and provide mechanical couplings between neighboring cells during embryonic development and tissue wound repair. This study determines the macromolecular conformations of AJ's cadherin-catenin-vinculin complex and reveals that this highly dynamic macromolecular complex utilizes the mechanosensory protein vinculin as the primary F-actin binding mode.

## INTRODUCTION

The adherens junctions (AJs) provide mechanical couplings between neighboring cells in tissues of multicellular organisms (1-3). Disassembly of the AJs results in the loss of cell polarity and contact inhibition, and permits cells to undergo an epithelial-to-mesenchymal transition (4,5). The dynamic remodeling of the AJs is necessary so that moving or migrating cells can continually break and remake adhesive bonds with neighboring cells during embryonic morphogenesis, organ development, tissue homeostasis, wound repair, and regeneration (6).

Submitted October 18, 2022, and accepted for publication April 27, 2023.

\*Correspondence: dcallaway@ccny.cuny.edu or zbu@ccny.cuny.edu

Editor: John Correia.

https://doi.org/10.1016/j.bpj.2023.04.026

© 2023 Biophysical Society.

The central component of the AJ is the cadherin. β-catenin·α-catenin (cadherin-catenin) complex and the cytoskeletal actin microfilaments (1,2). Cadherin is a single-helix transmembrane protein that employs its extracellular domain to form a homophilic transcellular bond with a cadherin from a neighboring cell (7). The intracellular domain of cadherin binds to \(\beta\)-catenin, and \(\beta\)-catenin in turn interacts with the actin-binding protein α-catenin, forming the cadherin-catenin complex that links to the cytoskeletal actin networks. The linkage of the cadherin-catenin complex to the actin cytoskeleton is essential for providing mechanical strength to cell-cell adhesion, and for sensing and transmitting mechanical tension between cells in quiescent tissues and during collective cell migration (6,8). Studies have shown that the interaction of the cadherin-catenin force with the actin microfilaments is force sensitive—mechanical forces are required for the cadherin-catenin complex to bind

effectively to F-actin (9,10). In cells, the mechanical forces are generated by the cytoskeletal actomyosin assemblies (11). The myosin motors produce pulling forces on the actin microfilaments, thereby causing tension within a filament as well as sliding movements between the filaments. The cadherin-catenin complex and the actomyosin assembly thus form an integral mechanosensing machinery that transmit mechanical signals between cells (12–15).

In addition to the core cadherin-catenin complex, the AJs associate with other intracellular proteins that are necessary for the stability and dynamic remodeling of the AJs (1,16– 18). In particular, vinculin is recruited to the AJs when cells are under recurrent high mechanical tensions, such as during cell collective migration, or in endothelium, cardiomyocytes, and skin cells (19–27). Vinculin is a cytoskeletal protein that plays important roles in cell adhesion, migration, and cell signaling (28-30). Vinculin is found at both cell-cell and cell-matrix adhesion sites. In cell-matrix focal adhesion, vinculin binds to talin, which in turn interacts with the transmembrane cell-matrix receptor integrin (31). Vinculin and talin together serve as adapters and mechanotransducers between the actomyosin bundle and integrin. In cell-cell adhesion, vinculin associates with the cadherin-catenin complex in an actomyosin-generated force-dependent manner (21-24,32). The interaction of the AJ with vinculin is vital for the proper development of heart and brain, and for maintaining skin stem cell quiescence (25–27). Vinculin is believed to serve as a force transducer and strengthens the AJs. However, the molecular mechanism by which vinculin modulates the cadherin-catenin complex to interact with F-actin is unclear.

Vinculin is composed of a head domain (Vh) and a tail actin-binding domain (VtABD) that are connected by a proline-rich linker (Fig.1 A). The Vh domain includes 4-helix bundle subdomains D1-D4. In the cytoplasm, vinculin adopts an autoinhibited conformation with the VtABD folded onto the Vh domain (38), which masks the ligand-binding sites in both the Vh and VtABD domains. Vinculin is activated when recruited to the AJs or to the cell-matrix focal adhesion sites (21,38). Multiple factors are thought to contribute to vinculin activation, including phosphorylation, actin-binding, phosphatidylinositol 4,5-bisphosphate binding, and mechanical force (39–42). Upon vinculin activation, the head-tail interactions are disrupted, and the head domain binds to the highly conserved vinculin-binding sequence (VBS) in α-catenin in cell-cell adhesion or in talin in cell-matrix adhesion, while VtABD binds to the actin microfilament (43,44).

Biochemical and x-ray crystallographic studies showed that the D1 subdomain of Vh binds to the VBS in the M1 subdomain of  $\alpha$ -catenin (Fig. 1 A), and that this binding results in the "unfurling" of M1 (45-47). Nevertheless, singlemolecule studies found that a force of about 5 pN is required to unfold α-catenin M1 to expose the cryptic VBS in M1 (48). A single-molecule force study showed that the vincu- $\lim \alpha$ -catenin bond has very high mechanical stability (49). Other studies found that vinculin forms a directionally asymmetric catch bond with F-actin (50). However, the structure of the whole cadherin-catenin-vinculin complex is not known, and it is not clear how the cadherin-catenin-vinculin complex interacts with F-actin. Currently, the available crystal structures of the AJ complex are the binary complexes of fragments from cadherin cytoplasmic domain · β-catenin, α-catenin · β-catenin complexes, and VBS from α-catenin bound to D1 of vinculin (45,46,51,52). The highly flexible and dynamic nature of the AJ complex, like many multidomain proteins or protein complexes with significantly disordered segments, poses challenges for structural studies (53,54).

We previously determined the nanoscale molecular structure and dynamics of the complex of  $\alpha$ -catenin  $\cdot$   $\beta$ -catenin E-cadherin cytoplasmic domain (ABE) using negative stain microscopy, small-angle x-ray scattering (SAXS), selective deuteration/small-angle neutron scattering (SANS), and neutron spin echo spectroscopy (33,55,56). The studies revealed that the ABE complex adopts an ensemble of flexible conformations with enhanced protein domain motions compared with  $\alpha$ -catenin alone in solution (33,55,56). The activated motion and an ensemble of flexible configurations of the mechanosensory ABD suggest the formation of an entropic trap in the cadherin-catenin complex, providing negative allosteric regulation that impedes the complex from binding to actin under zero force.

In this study, we identified that salt bridge interactions at the interface between Vh and Vt are the primary factor that locks vinculin in the head-tail autoinhibited configuration and generated a new type of vinculin activation mutant. Using the vinculin activation mutant, we reconstituted a complex of full-length vinculin bound to ABE (VABE), and determined the molecular conformation of the VABE complex using SAXS and selective deuteration/contrast variation SANS. The SANS study and analyses reveal that, upon binding vinculin, the VABE complex adopts an ensemble of conformations that are even more flexible and dynamic than the ABE complex alone, and the ensemble of full-length vinculin conformations adopt extended conformations with the vinculin actin-binding VtABD well separated from the Vh domain. Sedimentation F-actin binding experiments show that the VABE complex employs vinculin as the dominant F-actin binding mode and bundles F-actin. In the cellular context, the AJs likely switch between the weak and dynamic F-actin binding mode by the cadherin-catenin complex and the strong F-actin binding and bundling mode by the cadherin-catenin-vinculin complex to adapt to different mechanical requirements.

## **MATERIALS AND METHODS**

# Protein expression, purification, and complex reconstitution

The open reading frame cDNA of full-length human αE-catenin, full-length β-catenin, and the entire cytoplasmic

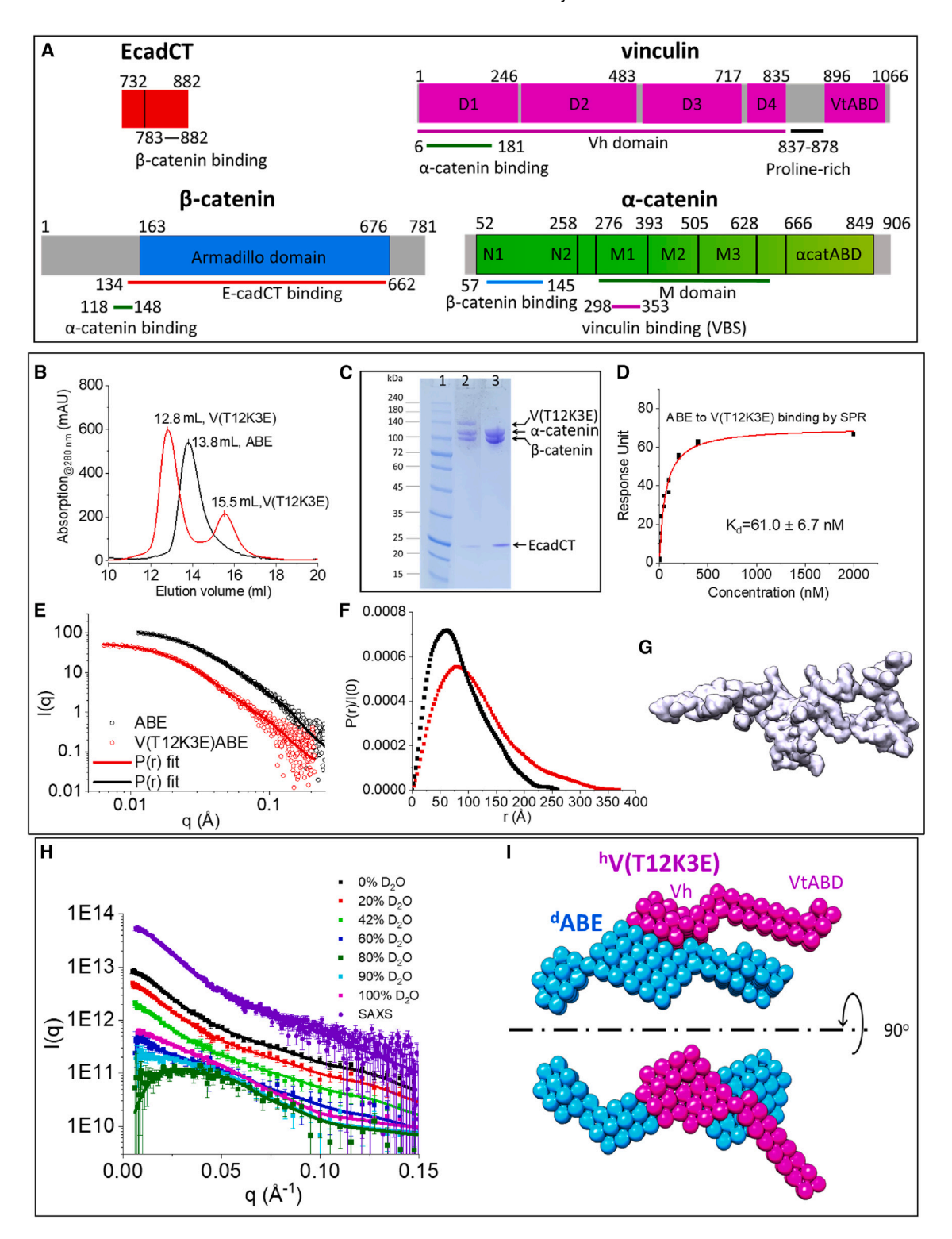


FIGURE 1 Reconstitution of full-length vinculin with ABE complex. (A) Primary structures of the cytoplasmic domain of E-cadherin (EcadCT), fulllength α-catenin, β-catenin, and vinculin. (B) SEC profiles of the ABE (black) and V(T12K3E)ABE (red) complexes, and excessive V(T12K3E) (red) during incubation, with the elution volumes of SEC peaks marked. (C) SDS-PAGE of V(T12K3E)ABE (lane 2) and ABE complex (lane 3) collected from the respective SEC peak fractions. (D) Binding curve of ABE to V(T12K3E) measured by SPR. The SPR binding sensorgrams are shown in Fig. S4 A. (E) SEC-SAXS data of ABE (black circle, from (33)) and V(T12KE)ABE (red circle). The lines are fits for computing P(r) functions. The SEC-SAXS profile of V(T12K3E)ABE and the Guinier plot are shown in Fig. S4, B and D. (F) P(r) functions of ABE (black) and V(T12K3E)ABE (red). Residuals of P(r) fit are shown in Fig. S4 C. (G) 3D shape of V(T12K3E)ABE ab initio reconstructed from the SAXS data using the program Gasbor (34). The 3D shapes of the complex reconstructed by other programs (35-37) are shown in Fig. S4 E. (H) Contrast variation SANS data of selectively

(legend continued on next page)

domain of E-cadherin, EcadCT (amino acid [aa] 732–882), vinculin head domains of aa 1–718 (Vh<sub>718</sub>), and aa 1–840 (Vh<sub>840</sub>) were subcloned in the pET-32a vector for bacterial expression. The vector contains an N-terminal 6xHis tag and a tobacco etch virus (TEV) protease cleavage sequence before the N-terminus of the expressed proteins. The cDNA of full-length human vinculin and vinculin activation mutants were cloned into the pET-21a vector with a C-terminus 6xHis tag for bacterial expression (GenScript, Piscataway, NJ).

The plasmids were transformed into Rosetta 2 (DE3) cells. After the cells were grown in at 37°C with the addition of 0.1 mg/mL ampicillin and 35  $\mu$ g/mL chloramphenicol. At optical density at 600 nm of about 0.6, 0.2 mM isopropyl  $\beta$ -D-1-thiogalactopyranoside was added to the cell culture to induce protein production for 5 h at 20°C. The cells were harvested by centrifugation at 5200  $\times$  g for 20 min, and the cell pellets were stored at -80°C.

For protein purification, the cell pellets were suspended in a binding buffer containing  $1\times$  phosphate-buffered saline (PBS) buffer (pH 7.4), 300 mM NaCl, 20 mM imidazole, and 0.1 mM phenylmethylsulfonyl fluoride. The cells were lysed by sonication on ice. The cell debris was clarified by centrifugation at  $10,000\times g$  for 20 min. The supernatant was passed through a HiTrap Chelating HP Ni column, and the column was washed with 15-20 column volumes of binding buffer. The protein was eluted with  $1\times$  PBS buffer (pH 7.4), 500 mM NaCl, and 500 mM imidazole. TEV was added to cleave the N-terminus thioredoxin-6xHis tag. The protein was further purified by size-exclusion chromatography (SEC) using a Superose 6 Increase 10/300 GL or a Superdex 200 Increase 10/300 GL column (Cytiva, Marlborough, MA). Both columns have a void volume of  $\sim$ 8.0 mL.

Details about reconstituting the ABE complex were described previously (33,56). The complexes of vinculin head domains with ABE or of full-length vinculin activation mutant with ABE were formed by incubating excessive amount of vinculin with the ABE complex. The VABE complexes were separated by SEC using a Superdex 200 Increase 10/300 GL column or a Superose 6 Increase 10/300 GL column.

Deuterated proteins were expressed in 85% D<sub>2</sub>O (v/v) M9 medium using a protocol described earlier (62,90–92). The procedures for purifying the deuterated proteins and reconstituting the selectively deuterated complexes were the same as those of the hydrogenated proteins. The software suite SASSIE (71) was used to compute the neutron scattering-length densities (SLD) of the buffer, the proteins, and the selectively deuterated complexes at different D<sub>2</sub>O volume fractions.

#### Surface plasmon resonance experiments

Surface plasmon resonance (SPR) experiments were performed on a Biacore X100 instrument (Cytiva). A Biacore CM5 Biosensor chip was activated by N-hydroxysuccinimide and N-ethyl-N'-[3-(diethylamino) propyl] carbodiimide. The ligand, Vh<sub>718</sub> or V(T12K3E), was dissolved at 5  $\mu$ g/mL in 10 mM sodium acetate (pH 4.9), and injected to coat the activated sensor chip surface in one of the two flow cells. The noncross-linked ligand was washed away and unoccupied sites were blocked with 1 M ethanolamine (pH 8.5). The control flow cell was activated and blocked without ligand injection. The analyte ABE complex was dialyzed in HBS-EP buffer (10 mM HEPES, [pH 7.4], 150 mM NaCl, 3 mM EDTA, 0.005% surfactant polysorbate 20) and injected in increasing concentrations over the ligand-coated surfaces at 30  $\mu$ L/min for 180 s. The dissociation time was 800 s. At the end of each injection-dissociation cycle, the sensor chip was regenerated with 50 mM triethylamine (pH 9.15), 4.0 M MgCl<sub>2</sub>, and HBS-EP buffer. SPR experiments were performed at 25°C. The Bia-evaluation software provided by the instrument manufacturer was used to obtain the equilibrium dissociation constant K<sub>d</sub> with a 1:1 binding model.

#### **SEC-SAXS** experiments

The SEC-SAXS experiments were performed at the Stanford Synchrotron Radiation Light Source (SSRL) Bio-SAXS Beamline 4-2. The experimental setup was as described previously (93). Details of SEC-SAXS data collection and analysis are listed in Table S1.

In total, 500 images were collected with 1-s exposure every 5 s at a 0.05 mL/min flow rate. After the 100th image (blank data collections), the x-ray shutter was closed until just before the sample was eluted to keep the sample cell clean from debris formed by x-ray radiation. An additional sample cell wash was executed during the shutter closure. Data reduction and initial analyses were performed using the BL4-2 automated SEC-SAXS data processing and analysis pipelines, SECPipe (https://www-ssrl.slac.stanford. edu/smb-saxs/node/1860) (93). It implements the program SASTOOL (https://www-ssrl.slac.stanford.edu/smb-saxs/ node/1914) and ATSAS AUTORG (59). The data were presented as I(q) versus q, where  $q = 4\pi \sin(\theta)/\lambda$ ,  $2\theta$  is the scattering angle, and  $\lambda$  is the wavelength of the x ray. After careful manual inspection, a total of five images were selected to generate the averaged profile for further analysis.

deuterated  ${}^{h}V(T12K3E){}^{d}A{}^{d}B{}^{d}E$  complex at different  $D_{2}O$  buffer volume fractions. The lines are fits to the scattering data for generating the two-phase ab initio 3D shape model. (I) Two-phase 3D shape of  ${}^{h}V(T12K3E){}^{d}A{}^{d}B{}^{d}E$  complex reconstructed from combined SAXS and contrast SANS data, assuming the deuterated ABE (cyan) bound to hydrogenated V(T12K3E) (magenta) as two different phases. The program MONSA from ATSAS 3.0 was used for the two-phase ab initio reconstruction (34).

## SANS experiments

SANS data were collected by the Bio-SANS instrument at the High Flux Isotope Reactor (HFIR) at Oak Ridge National Laboratory (94). A single configuration was used for Bio-SANS that placed the main detector at 7.0 m from the sample and the wing detector was fixed at 1.13 m from the sample. The wavelength was set to 6 Å with a relative wavelength spread ( $\Delta \lambda \lambda$ ) of 15%. This single configuration provides a q range of 0.007–0.80  $\mathring{A}^{-1}$ . All SANS measurements were performed at  $10 \pm 0.1$ °C with a Peltier temperature controller.

The facility software DRT-SANS (https://doi.org/10. 11578/dc.20220109.1) was used to reduce the data from the samples and from the backgrounds using standard procedures that correct for incident flux spectrum, sample transmission, and detector sensitivity, as well as the detector dark current, which represents electronic noise and natural sources of radiation. Then, the data were azimuthally averaged to generate I(q) versus q plots. Absolute intensity scaling for both configurations was done with a calibrated standard. The sample scattering was then corrected by subtracting solvent scattering to produce the final, reduced 1D

Before the SANS experiments, a PBS tablet (Thermo Fisher Scientific, Waltham, MA, USA) for making 500 mL 1× PBS buffer was soaked in 2 mL D<sub>2</sub>O and vacuum dried 5 times at 80°C to exchange the H in the tablet into D. The D-exchanged PBS tablet was dissolved with 500 mL 99.9% D<sub>2</sub>O, which was then mixed with H-unexchanged 1× PBS buffer at different volume fractions. The protein complex of 0.4 mL was dialyzed 5 times, each for 6-8 h, against 5 mL of 0, 20, 42, 60, 90, and 100% PBS D<sub>2</sub>O (v/v) buffer. The samples were loaded into 1-mm beam path cylindrical quartz cuvettes (Hellma, Müllheim, Germany) for measurement. Details of SANS data collection and analysis are listed in Table S2.

# SAXS and SANS data analysis and structural modeling

The distance distribution function P(r) was generated using the program GNOM (95) to obtain  $R_g$  and  $D_{max}$ . When computing P(r), the I(q) of q  $\leq 0.2$  Å $^{-1}$  was selected for fitting. A series of  $D_{max}$  values at which P(r) = 0 were tested, and the optimum  $D_{\text{max}}$  value with the minimum  $\alpha$ value and maximum total quality values was selected as the final solution.

The program Gasbor in ATSAS 3.0 was used to generate the ab initio shape of the V(T12K3E)ABE complex from the SAXS data. The program MONSA in ATSAS 3.0 was used to generate a multiphase ab initio shape, which combines the SEC-SAXS data of V(T12K3E)ABE and the SANS data of <sup>h</sup>V(T12K3E)<sup>d</sup>A<sup>d</sup>B<sup>d</sup>E collected at different volume fractions of D<sub>2</sub>O buffer, with the input R<sub>g</sub> value of <sup>d</sup>A<sup>d</sup>B<sup>d</sup>E in 42% D<sub>2</sub>O and the R<sub>g</sub> value of hvinculin(T12K3E) in 100% D<sub>2</sub>O, and the deuteration level of <sup>d</sup>A<sup>d</sup>B<sup>d</sup>E from neutron SLD contrast calculations.

The program suite SASSIE (71) was used for Monte Carlo simulation structure generations, neutron SLD calculations of the selectively deuterated protein complexes and the buffer, comparison with experimental SANS data, and for selecting the conformations. Before Monte Carlo simulations, the crystal structure of the nearly full-length vinculin (PDB: 1tr2) was used as the starting structure, and the program I-TASSER (68) was used to rebuild the flexible loops or linkers that are missing in the crystal structure. The all-atomic structural coordinates of the ABE complex derived from SAXS and SANS (33) were used as the starting structure to dock with vinculin. Multiple rounds of simulations were performed for each component with each round of 5000 to 10,000 trial attempts. Details about the steps of Monte Carlo simulations and conformation selection of the complex at different contrasts of SANS are described in supporting experimental procedures.

# Protein complex molecular mass measurements using contrast variation SANS

At various D<sub>2</sub>O concentrations, the oligomeric state and stoichiometry of the complexes can be determined by contrast variation SANS:

$$\frac{1}{\bar{\nu}} \left[ \frac{100 * I(0) * N_A}{c} \right]^{0.5} = \left[ \frac{\rho_D M_D + \rho_H M_H}{(M_D + M_H)^{0.5}} - \rho_o (M_D + M_H)^{0.5} \right]$$
(1)

where I(0) is the forward scattering intensity on absolute scale, c is the protein concentration in mg/mL,  $\overline{\nu}$  = 0.73 cm<sup>3</sup>/g is the partial specific volume of the complex,  $N_A$  is Avagadro's number,  $\rho_D$  and  $\rho_H$  are the neutron SLD of the deuterated component and the hydrogenated component, respectively,  $\rho_o$  is the neutron SLD of the buffer, and M<sub>D</sub> and M<sub>H</sub> are the molecular masses of the deuterated and hydrogenated components, respectively. Eq. 1 was rederived from an earlier version described in (65).

## Sedimentation F-actin binding experiments

The actin protein (>99 pure) purified from rabbit skeletal muscle was purchased from Cytoskeleton (Denver, CO), and the F-actin binding experiments follow the protocol provided by the vendor with some modifications. First 1 mg actin was first dissolved in 0.5 mL ice-cold water to make a 2 mg/mL stock solution. The actin solution was then dialyzed against the general actin buffer (5 mM Tris-HCl [pH 8.0], 0.2 mM CaCl<sub>2</sub>, 0.2 mM ATP) overnight. After dialysis, the actin solution volume was adjusted to 0.9 mL with the

addition of general actin buffer. To initialize actin polymerization, 0.1 mL or a 10% volume fraction of 10× actin polymerization buffer (100 mM Tris-HCl [pH 7.5], 1000 mM KCl, 20 mM MgCl<sub>2</sub>, 10 mM ATP, 10% glycerol) was added to the actin solution to initiate polymerization, and the solution was incubated for 1 h at room temperature. The final F-actin stock contained  $\sim$ 23.8  $\mu$ M actin.

The ligand (protein or protein complex, positive or negative control) was first concentrated and exchanged into 10 mM Tris-HCl (pH 7.5) and 150 mM NaCl by dialysis to remove EDTA in the FPLC purification buffer. The ligand concentration was then adjusted to 50  $\mu$ M. A 2.4- $\mu$ L aliquot of the ligand stock solution was added to 40 µL F-actin solution, and the reaction volume was adjusted to 50  $\mu$ L by adding 7.6  $\mu$ L 1× F-actin buffer. The molar ratio of ligand to actin was 1:8. The ligand/F-actin mixture was incubated at room temperature for 20 min before centrifugation.

The incubated mixture was centrifuged at 1,500,00  $\times$  g for 1.5 h at room temperature using a Beckman Coulter air-driven ultracentrifuge with an A-100/18 rotor. After centrifugation, 25 µL of the supernatant was pipetted out of the centrifuge tube and mixed with 25  $\mu$ L of 2× SDS-PAGE sample buffer. The remaining supernatant was blotted off with a filter paper. The F-actin pellet was then dissolved in 25  $\mu$ L deionized water and mixed with 25  $\mu$ L of 2× SDS-PAGE sample buffer. The supernatant and pellet were subjected to SDS-PAGE. The SDS-PAGE gel was documented, and the intensities of the gel bands were analyzed using the program Image J (96).

#### **RESULTS**

# Reconstituting full-length vinculin bound to the cadherin-catenin complex

The reconstitution, structure and dynamics of the ABE complex have been described previously (33). We first examined the interaction of the vinculin head domain Vh<sub>718</sub> (aa 1-718) with the ABE complex. Incubating ABE with excessive Vh<sub>718</sub> forms a discrete complex that is larger than ABE as shown by SEC (Fig. S1 A, B, and E–G). The dissociation constant of Vh<sub>718</sub> to ABE binding is  $K_d = 60.1 \pm$ 8.7 nM as measured by SPR (Fig. S1 C and D). Thus, Vh<sub>718</sub> binds ABE with high affinity.

Incubation and SEC experiments indicate that the wildtype full-length vinculin does not bind ABE. This result supports previous findings that vinculin adopts an autoinhibited conformation (57). Previous studies reported activation mutants of vinculin: vinculin-T12 mutant (D974A, K975A, R976A, and R978A) and vinculin-T12K-A974K mutant (D974K, K975A, R976A, and R978A), both with mutations in the VtABD (34,58). However, our SEC/SDS-PAGE analysis shows that neither of these two vinculin mutants binds ABE effectively to form a discrete complex, even though ABE can incorporate a trace amount of vinculin-T12 or vinculin-T12-A974K after incubating ABE with an excessive amounts of these two full-length vinculin mutants, respectively (Fig. S2 A and B).

By examining the crystal structure of the full-length vinculin (PDB: 1tr2), we identified two patches of salt bridges at the interface between the Vh and VtABD domains (Fig. S3 A). The residues involved in forming the salt bridges are E14 in head D1 with K996 in tail VtABD, and E28 and E29 in D1 with K944 and K945 in VtABD. We speculated that the ionic interactions may contribute to locking the Vh and VtABD domains in the autoinhibited conformation, and thus mutated residues K944E/R945E/K996E in VtABD in addition to the T12 mutations. This new fulllength vinculin mutant is named V(T12K3E).

SANS experiments suggest that, in solution, the V(T12K3E) mutant has altered conformation compared with that of the wild-type vinculin (vinculin(wt)) (Fig. S3) B-D; Table 1). The Guinier plots and the length distribution function P(r)s show that the V(T12K3E) mutant is larger and more expanded than vinculin(wt). The radius of gyration  $R_g$ increases from 34.5  $\pm$  0.7 Å for vinculin(wt) to 44.0  $\pm$  0.6 Å for V(T12K3E), and the maximum dimension D<sub>max</sub> expands from 108 Å for vinculin(wt) to 147 Å for V(T12K3E). The SANS experiments further show that vinculin(wt) adopts the same compact conformation in solution as that in the crystal structure when comparing the P(r) from the solution SANS data of vinculin(wt) with that calculated from the crystal structure (PDB: 1tr2) (Fig. S3 B and D). The SANS results thus provide structural evidence that the salt bridge disrupting mutations alter the conforamtion of full-length vinculin to make the protein more open in solution.

Incubating V(T12K3E) with the ABE complex forms a discrete complex that is larger than ABE (Fig. 1 B and C). V(T12K3E) has the same binding affinity for the ABE complex as the Vh domain with  $K_d = 61.0 \pm 6.7$  nM (Figs. 1D and S4 A). V(T12K3E) thus mimics an activated and open full-length vinculin that binds ABE, which enables us to reconstitute a complex of full-length VABE, V(T12K3E) ABE, for structural studies by SAXS and SANS. We later generated a vinculin mutant V(E3K) with all mutations E14K/E28K/E29K only in the Vh domain for F-actin binding experiments without perturbing the actin-binding function of VtABD (Fig. S2 E). This V(E3K) also binds to ABE to form a discrete V(E3K)ABE complex in SEC (Fig. S3 E and F). Thus, our mutagenesis, SANS, and binding experiments together show that the two patches of ionic interactions formed at the interface between Vh and VtABD are the primary factors to lock the full-length vinculin in the head-tail autoinhibited conformation.

# The 3D shape and stoichiometry of the VABE complex

SEC-SAXS shows that the V(T12K3E)ABE complex is larger than the ABE complex, with  $R_g = 92.0 \pm 2.5 \text{ Å}$  and

TABLE 1 Summary of  $R_g$  and  $D_{max}$  measured by SEC-SAXS and SANS

Complex	Methods	Concentration (mg/mL)	$R_g*(\mathring{A})$	D <sub>max</sub> (Å)	Calculated Mw (kDa)	Measured Mw (kDa)
VABE complex						
Vh <sub>718</sub> ABE	SEC-SAXS	see Table S1	90.4 ± 1.9	354 ± 5	281.0	277.6 ± 15.4**
V(T12K3E)ABE	SEC-SAXS	see Table S1	$92.0 \pm 2.5$	$370 \pm 5$	320.7	
$^{h}V(T12K3E)^{d}A^{h}B^{h}E$	SANS, $0\%$ D <sub>2</sub> O	4.18	$94.8 \pm 2.5$	$369 \pm 5$		
$^{\text{h}}\text{V}(\text{T}12\text{K}3\text{E})^{\text{d}}\text{A}^{\text{d}}\text{B}^{\text{d}}\text{E}$	SANS, 0% D <sub>2</sub> O	3.34	94.5 ± 2.1	$375 \pm 5$		333.3 ± 50.8**
ABE conformation						
ABE***	SEC-SAXS		$69.3 \pm 2.8$	$260 \pm 5$	202.7	195.1 ± 10.1**
<sup>h</sup> V(T12K3E) <sup>d</sup> A <sup>d</sup> B <sup>d</sup> E	SANS, 42% D <sub>2</sub> O	3.28	$89.9 \pm 2.6$	$352 \pm 5$		
for ABE in VABE						
α-Catenin conformation						
α-Catenin monomer****	SEC-SAXS		43.7 ± 1.1	150 ± 5		
<sup>d</sup> AhBhE	SANS, 42% D <sub>2</sub> O		$56.7 \pm 0.9$	$200 \pm 5$		
for α-catenin in ABE***						
<sup>h</sup> V(T12K3E) <sup>d</sup> A <sup>h</sup> B <sup>h</sup> E	SANS, 42% D <sub>2</sub> O	3.71	$70.3 \pm 1.6$	$246 \pm 5$		
for α-catenin in VABE	_	_				
β-Catenin conformation						
<sup>d</sup> V(T12K3E) <sup>d</sup> A <sup>h</sup> B <sup>d</sup> E	SANS, 100% D <sub>2</sub> O	2.94	56.2 ± 2.2	215 ± 5		
for β-catenin in VABE	, <u>-</u>					
$^{d}A^{h}B^{d}E$	SANS, 100% D <sub>2</sub> O		$51.9 \pm 1.8$	$220 \pm 5$		
for $\beta$ -catenin in ABE***						
Vinculin conformation						
Vinculin(wt) in solution	SANS, 100% D <sub>2</sub> O	5.56	$34.5 \pm 0.7$	108 ± 5		
V(T12K3E) in solution	SANS, 100% D <sub>2</sub> O	2.40	$44.0 \pm 0.6$	$147 \pm 5$		
$^{d}V(T12K3E)^{h}A^{h}B^{h}E$	SANS, 42% D <sub>2</sub> O	2.21	$69.6 \pm 3.9$	$240 \pm 10$		
for V(T12K3E) in VABE						

<sup>\*</sup>From P(r) analysis.

 $D_{max} = 370 \,\text{Å}$  for V(T12K3E)ABE compared with ABE with  $R_g = 69.3 \pm 2.8 \,\text{Å}$  and  $D_{max} = 260 \,\text{Å}$  (Figs. 1 E, F, and S4 B-F; Table 1. We restored the ab initio 3D shape of V(T12K3E)ABE from the SAXS data using the GASBOR program in the ATSAS 3.0 suite (59) (Fig. 1 G), and using other ab initio programs including DENSS (35), DENSS Multiple (36), and DAMMIF (37) (Fig. S4 E). The 3D shapes restored from the different programs all show that the V(T12K3E)ABE complex is elongated with a lobe protruding from the middle of the complex.

To resolve the locations of vinculin and ABE, respectively, within the V(T12K3E)ABE complex, we reconstituted the hydrogenated V(T12K3E) bound to the deuterated ABE (<sup>d</sup>A<sup>d</sup>B<sup>d</sup>E) to form a selectively deuterated <sup>h</sup>V(T12K3E)<sup>d</sup>A<sup>d</sup>B<sup>d</sup>E complex, and performed contrast variation SANS measurements on this selectively deuterated complex (Figs. 1 *H, I,* and S5 *A-C*). The parameters measured by SANS are the same as those measured by SAXS. However, with the aid of selective deuteration and contrast variation, SANS can further resolve the conformation of an individual component within a multicomponent complex as well as the molecular mass and stoichiometry

(Fig. S6 A and B) and the overall architecture of the complex (60-63).

Forward scattering intensity I(0) measurements at different contrasts provide the absolute molecular mass of a macromolecular complex that is independent of protein size and shape (Eq. 1) (Fig. S6 A and B) (33,64,65). The contrast variation SANS measured molecular mass of the  ${}^{\rm h}V({\rm T}12{\rm K}3{\rm E})^{\rm d}A^{\rm d}B^{\rm d}{\rm E}$  complex is Mw = 333.2  $\pm$  50.8 kDa (Fig. S6 A). This measured absolute molecular mass is close to the theoretical molecular mass of Mw = 320.7 kDa of a 1:1:1:1 V(T12K3E)ABE complex. Using the same method, we measured the molecular mass of the  ${}^{\rm d}Vh_{718}{}^{\rm h}A^{\rm h}B^{\rm h}E$  complex to be Mw = 277.6  $\pm$  15.4 kDa (Fig. S6 B), which is close to the theoretical Mw = 281.0 kDa of a 1:1:1:1 Vh<sub>718</sub>ABE complex (Table 1).

Using the SAXS and SANS data at different contrasts shown in Fig. 1 *H*, we restored the two-phase ab initio 3D shape of the V(T12K3E)ABE complex using the program MONSA in ATSAS 3.0 (59), assuming that the complex is composed of a hydrogenated V(T12K3E) phase and a deuterated ABE phase. The 3D shape of the complex shows that both the deuterated ABE and the hydrogenated

<sup>\*\*</sup>From contrast variation SANS, Fig. S6.

<sup>\*\*\*</sup>From (56).

<sup>\*\*\*\*</sup>From (57).

V(T12K3E) phases are elongated, with a compact lobe of the hydrogenated V(T12K3E) anchored in the middle of the deuterated ABE phase, and a V(T12K3E) tail protrudes from the middle of ABE (Fig. 1 I). These preliminary ab initio 3D shape analyses of the SAXS and SANS data reveal the overall conformation of the V(T12K3E)ABE complex as well as the location of V(T12K3E) and ABE in the V(T12K3E)ABE complex.

Previously we combined negative stain EM 2D classification with SAXS and SANS analyses to reveal that the ABE complex is dynamic and adopts an ensemble of flexible domain conformations (33,55). However, upon binding to vinculin, the VABE complex becomes even more flexible and highly dynamic, which makes it difficult to collect good quality negative stain images for 2D classification of the complex. In the following, we employ a hybrid approach, combining SANS with Monte Carlo simulations to provide all-atomistic molecular models of the conformations of full-length vinculin, α-catenin, β-catenin, and the whole VABE complex. We further compare the conformation distribution of vinculin, α-catenin, and β-catenin in the highly dynamic VABE complex using the ensemble optimization EOM analyses (66,67) of the SANS data.

# V(T12K3E) adopts extended conformations when bound to the ABE complex

SANS suggests that the V(T12K3E) mutant is more expanded than vinculin(wt), while vinculin(wt) has the same compact conformation as that shown in the crystal structure (Figs. 2 A–C and S7 A–C, black and blue data). To reveal the conformation of V(T12K3E) as part of the VABE complex, we reconstituted the selectively deuterated <sup>d</sup>V(T12K3E)<sup>h</sup>A<sup>h</sup>B<sup>h</sup>E complex (Figs. 2 A-C and S7 A-C, red data). In 42% D<sub>2</sub>O buffer at the contrast-matching point of the hydrogenated ABE, SANS measures the conformation of the deuterated V(T12K3E) within the complex. Contrast-matching SANS indicates that the conformation of V(T12K3E) as part of the complex is even more extended than V(T12K3E) alone in solution, as exhibited by P(r) with  $R_g = 69.6 \pm 3.9 \text{ Å}$  and  $D_{max} =$ 240 Å (Fig. 2 B; Table 1). The normalized Kratky plot (69,70) suggests that the V(T12K3E) structure is more open in the complex than V(T12K3E) in solution (Fig. 2 C). Comparing the SANS data of vinculin(wt), and V(T12K3E) in solution and in the V(T12K3E)ABE complex thus shows that the salt bridge disrupting V(T12K3E) mutant is partially open in solution, and becomes extended when bound to the ABE complex.

To provide an all atomistic structural model of V(T12K3E) in solution, we performed Monte Carlo simulations on the full-length vinculin structure (PDB: 1tr2) using the program SASSIE (71). During simulations, the linkers between D1-D2 (aa 250-254), D2-D3 (aa 484-492), D3-D4 (aa 717-723), and D4-VtABD (aa 836-896) were assumed to be flexible and the simulations were directed with the protein having an  $R_g = 44.0 \text{ Å}$  as determined experimentally by SANS (Table 1). Details about the Monte Carlo simulation and conformation selections against SANS data at different contrasts are described in supporting experimental procedures. The Monte Carlo simulation generated a pool of full-length vinculin structures of differently open conformations. The theoretical SANS curves computed from this pool of vinculin structures were compared against the experimental SANS data of V(T12K3E) in 100% D<sub>2</sub>O buffer solution (Figs. 2 A, blue data and blue line, and S7 D). The structures that fit the experimental SANS data with  $\chi^2 \le 1.2$  were selected as the acceptable ensemble of V(T12K3E) conformations in solution (Fig. 2 G). Fig. 2 E shows one representative selected structural model of V(T12K3E) in solution of a best fit structure to the SANS data, which shows a partially open conformation with VtABD unlocked from the Vh domain.

Monte Carlo simulations were also performed on vinculin to provide a structural model of vinculin residing in the V(T12K3E)ABE complex, assuming that the linkers between D1-D2, D2-D3, D3-D4, and D4-VtABD are flexible and the simulations were directed with V(T12K3E) having an of  $R_g = 69.5 \text{ Å}$  as determined experimentally by SANS (Table 1). The simulation-generated pool of structures were then compared against the SANS data of <sup>d</sup>V(T12K3E)<sup>h</sup>A<sup>h</sup>B<sup>h</sup>E in 42% D<sub>2</sub>O buffer (Figs 2 A, red data, and S7 E). The simulation-generated vinculin structures with  $\chi^2 \le 1.2$  fits to the SANS data were accepted the conformation ensemble in the V(T12K3E)ABE complex (Fig. 2 H). Fig. 2 F shows one representative structure of V(T12K3E) structure from the ensemble, with  $R_g$ 68.6 Å and  $\chi^2 = 0.797$ , in which VtABD is further separated away from the Vh domain as compared with V(T12K3E) alone in solution.

To estimate the conformational distribution of V(T12K3E) in solution and in the V(T12K3E)ABE complex, we performed ensemble analyses of the SANS data using the program EOM (66,67) (Fig. S8 A and B). The EOM analyses suggest that the conformation of V(T12K3E) in solution has two populations, one major population of 79.6% adopts a compact conformation with  $R_g$  peaked at 42.5 Å and  $D_{max}$  at 130–155 Å, and a minor population of 20.4% of extended conformations with R<sub>g</sub> peaks at 59.4 Å and D<sub>max</sub> at 212.5 Å (Fig. S8 B). Nevertheless, even the compact population has  $R_{\rm g}$  and  $D_{\rm max}$  values that are larger than the vinculin(wt) but are close to P(r) analyses of V(T12K3E) in solution, suggesting that the compact population of V(T12K3E) is partially open in solution. In the V(T12K3E)ABE complex, the conformation of V(T12K3E) is predominantly extended, with R<sub>g</sub> ranging between 57 and 66 Å and  $D_{max}$  between 182 and 214 Å. The EOM analyses thus reach the same conclusion as ensemble averaged analyses of the SANS data that the

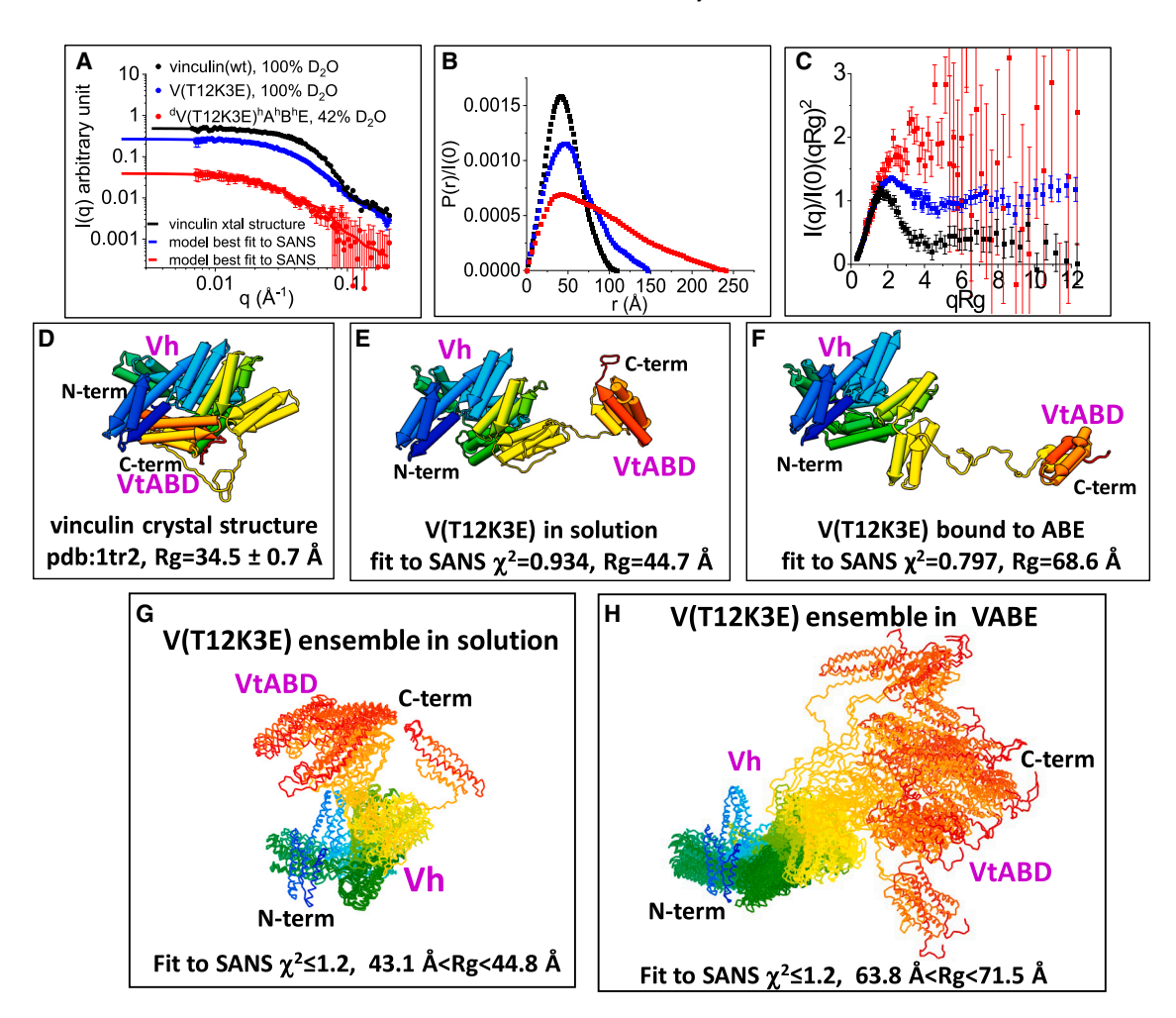


FIGURE 2 Conformation of full-length vinculin in solution and in complex to ABE. (A) SANS data of vinculin(wt) in 100% D<sub>2</sub>O (black), V(T12K3E) in 100% D<sub>2</sub>O (blue), and <sup>d</sup>V(T12K3E) in the <sup>d</sup>V(T12K3E)<sup>h</sup>A<sup>h</sup>B<sup>h</sup>E complex in 42% D<sub>2</sub>O (red). Guinier plots are shown in Fig. S7 A. The black line is the theoretical scattering curve computed from the crystal structure of vinculin(wt) (PDB: 1tr2) with missing loops reconstructed using the program I-TASSER (68). The blue and red lines are the best fits of the Monte Carlo simulation-generated structures that are selected against SANS data of V(T12K3E) in 100% D<sub>2</sub>O and of <sup>d</sup>V(T12K3E)<sup>h</sup>A<sup>h</sup>B<sup>h</sup>E complex in 42% D<sub>2</sub>O, respectively. (B) P(r) functions of vinculin(wt) in 100% D<sub>2</sub>O (black), V(T12K3E) in 100% D<sub>2</sub>O (blue), and <sup>d</sup>V(T12K3E)<sup>h</sup>A<sup>h</sup>B<sup>h</sup>E in 42% D<sub>2</sub>O (red). Quality of P(r) fit is shown in Fig. S7, B and C. (C) Normalized Kratky plot of vinculin(wt) in 100% D<sub>2</sub>O (black), V(T12K3E) in 100% D<sub>2</sub>O (blue), and <sup>d</sup>V(T12K3E)<sup>h</sup>A<sup>h</sup>B<sup>h</sup>E in 42% D<sub>2</sub>O (red). (D) Crystal structure of vinculin(wt) (PDB: 1tr2). (E) One representative V(T2K3D) structure model of V(T12K3E) in 100% D2O from the ensemble of Monte Carlo simulation generated structures that are selected by the SANS data shown in (G). This structure has  $R_g = 44.7$  Å and lowest fitting  $\chi^2 = 0.934$  to SANS data. (F) One representative structural model of V(T12K3E) as part of the V(T12K3E)ABE complex from the ensemble of simulation-generated structures that are selected by SANS data of <sup>d</sup>V(T12K3E)- $^hA^hB^hE$  complex in 42%  $D_2O$  shown in (H). This structure has  $R_g=68.6$  Å and lowest fitting  $\chi^2=0.797$ . (G) Ensemble of V(T12K3E) conformations in solution selected by fitting the Monte Carlo simulation-generated pool against the SANS data of V(T12K3E) in 100%  $D_2O$ , with the range  $\chi^2$  and  $R_g$  values of the ensemble specified. (H) Ensemble of V(T12K3E) conformations in the V(T12K3E)ABE complex selected by fitting the Monte Carlo simulation-generated pool against the SANS data of  $^{d}V(T12K3E)^{h}A^{h}B^{h}E$  in 42%  $D_{2}O$ , with the ensemble  $\chi^{2}$  and  $R_{g}$  values specified.  $\chi^{2}$  versus  $R_{g}$  plots are shown in Fig. S7, D and E.

vinculin activation mimic V(T12K3E) is partially open in solution and that, once V(T12K3E) is bound to ABE, V(T12K3E) adopts extended and open conformations.

# $\alpha$ -Catenin unfolds into two separate lobes in the **VABE** complex

Previous studies show that, in the ABE complex,  $\alpha$ -catenin adopts more open conformations and is more dynamic than  $\alpha$ -catenin in solution (33,55,56). To reveal the conformation of α-catenin within the V(T12K3E)ABE complex, we reconstituted the hydrogenated V(T12K3E) bound to deuterated α-catenin, hydrogenated β-catenin, and hydrogenated EcadCT to form a selectively deuterated <sup>h</sup>V(T12K3E)-<sup>d</sup>A<sup>h</sup>B<sup>h</sup>E complex. In 42% D<sub>2</sub>O at the contrast-matching point of the hydrogenated components, SANS only measures the conformation of the deuterated α-catenin within the <sup>h</sup>V(T12K3E)<sup>d</sup>A<sup>h</sup>B<sup>h</sup>E complex (Figs. 3 A–C and S9 A and B, blue data). As a comparison, the scattering data of α-catenin monomer in solution (black data) and in the

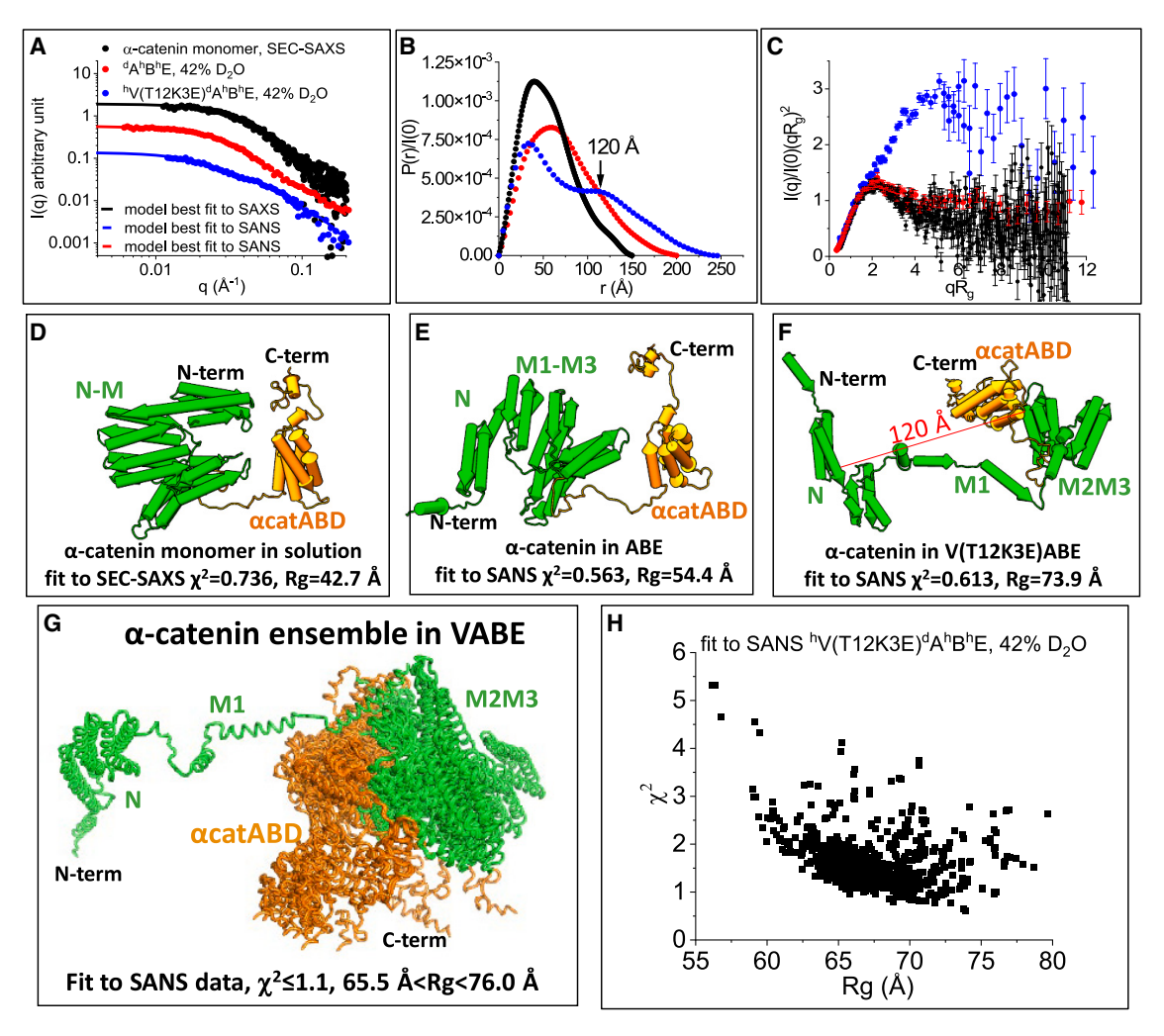


FIGURE 3 α-Catenin conformation in solution, in ABE, and in VABE. (A) SEC-SAXS data of α-catenin monomer in solution (*black*, data taken from (56)), SANS data of  $^{d}A^{h}B^{h}E$  complex in 42% D<sub>2</sub>O (*red*, data taken from (33)), and SANS data of  $^{h}V(T12K3E)^{d}A^{h}B^{h}E$  complex in 42% D<sub>2</sub>O (*blue*). Guinier plots are shown in Fig. S9 A. The lines are the best fit of the theoretical curves computed from the Monte Carlo simulation-generated structures that are selected against the SANS data. (B) P(r) functions of α-catenin monomer in solution from SAXS (*black*),  $^{d}A^{h}B^{h}E$  complex from SANS in 42% D<sub>2</sub>O (*red*), and  $^{h}V(T12K3E)^{d}A^{h}B^{h}E$  complex from SANS in 42% D<sub>2</sub>O (*blue*). Quality of P(r) fit is shown in Fig. S9 B. (C) Normalized Kratky plots, colors are the same as in (A or B). (D–F) Representative structural models of α-catenin from the ensemble of simulation-generated structures that are selected against SAXS or SANS data. (D) α-Catenin monomer against SAXS data. The shown structure has  $R_g = 42.7$  Å and lowest fitting  $\chi^2 = 0.736$  taken from (56). (E) α-Catenin in the ABE complex against SANS data of  $^{d}A^{h}B^{h}E$  in 42% D<sub>2</sub>O. The shown structure has  $R_g = 54.4$  Å and lowest  $\chi^2 = 0.563$  taken from (33). (F) α-Catenin in the V(T12K3E)ABE complex against SANS data of  $^{h}V(T12K3E)^{d}A^{h}B^{h}E$  in 42% D<sub>2</sub>O. The shown structure has  $R_g = 73.9$  Å and lowest fitting  $\chi^2 = 0.613$ . αcatABD is highlighted in orange. (G) Ensemble of α-catenin conformations in the V(T12K3E)ABE complex selected against SANS data of  $^{h}V(T12K3E)^{d}A^{h}B^{h}E$  in 42% D<sub>2</sub>O.  $\chi^2$  versus  $\chi^2$  versus  $\chi^2$  plot of fitting Monte Carlo simulation-generated structures against SANS data of  $^{h}V(T12K3E)^{d}A^{h}B^{h}E$  in 42% D<sub>2</sub>O.  $\chi^2$  versus  $\chi^2$  versus  $\chi^2$  versus  $\chi^2$  versus  $\chi^2$  versus  $\chi^2$  complex are shown Fig. S9, C and D.

ABE complex (red data) from previous studies (33,55,56) are also shown in Figs. 3 A–C and S9 A and B). The contrast-matching SANS data indicates that  $\alpha$ -catenin undergoes significant conformational changes in the V(T12K3E)ABE complex compared with  $\alpha$ -catenin in the ABE complex (Fig. 3 A–C). The normalized Kratky plot shows that the overall structure of  $\alpha$ -catenin becomes even more open in the V(T12K3E)ABE complex than in the ABE complex (Fig. 3 C). P(r) indicates that  $\alpha$ -catenin is unfolded into two distinct lobes that are separated by about 120 Å (Fig. 3 B, blue data).

To provide a structural model of  $\alpha$ -catenin residing in the V(T12K3E)ABE complex, we first docked the open structure of full-length vinculin obtained from Fig. 2 F to the VBS of  $\alpha$ -catenin in the ABE complex, using the coordinates of ABE obtained from SANS (33) and the available crystal structure of vinculin D1 domain complexed to the  $\alpha$ -catenin VBS fragment (PDB: 4EHP) as a template. Docking vinculin to the  $\alpha$ -catenin VBS requires dislodging of the helix-turn-helix (aa 298–353) from the M1 subdomain and the unfolding of this helix-turn-helix to align with vinculin D1 as defined by the crystal structures (45,46). Docking was performed using

the Tools 

Structure Comparison module in UCSF Chimera (72). Monte Carlo simulations were performed on  $\alpha$ -catenin, assuming the flexible regions in  $\alpha$ -catenin: aa 1–53 in the N-terminus, aa 261–277 connecting the N2-M1 domains, aa 291-297 and aa 354-362 in the M1 domain, aa 630-682 connecting the M3 and acatABD domains, and aa 849-906 in the C-terminal tail of acatABD. The theoretical SANS curves of the simulation-generated structures were computed, assuming that  $\alpha$ -catenin is deuterated, but vinculin,  $\beta$ -catenin, and EcadCT are hydrogenated, and the complex is in 42% D<sub>2</sub>O buffer. The calculated scattering curves were compared against the contrast-matching SANS data of <sup>h</sup>V(T12K3E)<sup>d</sup>A<sup>h</sup>B<sup>h</sup>E in 42% D<sub>2</sub>O (Fig. 3 A, blue data, and H), which generates an ensemble of acceptable conformations with a selection criterion of  $\chi^2$  < 1.0 (Fig. 3 G and H). Fig. 3 F shows one representative selected  $\alpha$ -catenin structure within the complex, with  $R_g = 73.9 \text{ Å}$  and  $\chi^2 =$ 0.613 against the SANS data. As comparison, the conformation of α-catenin in solution and in the ABE complex obtained from Monte Carlo simulations and scattering data selection are shown in Fig. 3 D and E, respectively.

Previous x-ray crystallographic studies showed that, upon binding to the D1 subdomain of vinculin, the α-catenin M1 subdomain becomes unfurled to expose the VBS in M1 for vinculin binding (45,46). The SANS experiment and simulations here show that vinculin-binding and the unraveling of the α-catenin M1 subdomain cause significant changes in the global conformation of the full-length  $\alpha$ -catenin. As a result of vinculin binding, α-catenin becomes separated into two distinct lobes that are connected by a long bridge (Fig. 3 F). The first lobe is composed of the N1N2 domains that bind \(\beta\)-catenin, and the second lobe includes the M2M3-αABD domains, with the two lobes being about 120 Å apart. The second lobe of M2-αcatABD can further be divided into two sublobes composed of M2M3 and αcatABD, with the center-of-mass distance between M2M3 and acatABD being about 40 Å. The long bridge between the two lobes is composed of the N2-M1 linker and the VBS that is bound to  $V_h$ .

A previous study revealed that α-catenin in the ABE complex adopts an ensemble of flexible conformations (33). Here, the SANS data and analyses in Fig. 3 A–H show that, upon binding to vinculin,  $\alpha$ -catenin becomes even more flexible. EOM analysis of the SANS data indicates a wider conformation distribution of α-catenin in the VABE complex than in the ABE complex (Fig. S10 A and B). The flexible linkers between N2-VBS, VBS-M2, and M3-αcatABD are responsible for the flexible and wide conformational distribution of  $\alpha$ -catenin in the V(T12K3E)ABE complex.

# Two distinct conformation populations of β-catenin in the V(T12K3E)ABE complex

To resolve the conformation of  $\beta$ -catenin within the V(T12K3E)ABE complex, we reconstituted the hydrogenated β-catenin in the selectively deuterated <sup>d</sup>V(T12K3E)-<sup>d</sup>A<sup>h</sup>B<sup>d</sup>E complex. SANS in 100% D<sub>2</sub>O measures the conformation of the hydrogenated β-catenin at the contrastmatching point of the deuterated components in the complex (Figs. 4 A–C and S11 A–C, red data). P(r) indicates that the overall conformation of β-catenin in the V(T12K3E)ABE complex is not significantly different from that of  $\beta$ -catenin in the ABE complex, except a small shoulder at r  $\sim$  175 Å that becomes distinct for  $\beta$ -catenin in the  ${}^{d}V(T12K3E)$ -<sup>d</sup>A<sup>h</sup>B<sup>d</sup>E complex (Fig. 4 B). However, the Kratky plot suggests that \( \beta\)-catenin is more extended or more open in the V(T12K3E)ABE complex than in the ABE complex (Fig. 4 C).  $R_g$  of  $\beta$ -catenin in the V(T12K3E)ABE complex increases to 56.2  $\pm$  2.2 from  $R_g = 51.9 \pm 1.8$  Å in the ABE complex (Table 1). The altered  $\beta$ -catenin structure is likely due to the interaction of  $\beta$ -catenin with vinculin as reported by a previous biochemical study (73).

Monte Carlo simulations on β-catenin in the VABE complex were performed assuming that aa 1–163 residues at the N-terminus and aa 681–781 residues at the C-terminus are flexible, and the simulation-generated structures were selected against the contrast-matching SANS data of the deuterated <sup>d</sup>V(T12K3E)<sup>d</sup>A<sup>h</sup>B<sup>d</sup>E complex in 100% D<sub>2</sub>O to obtain an ensemble of  $\beta$ -catenin conformations in the VABE complex (Fig. 4 A, F, and G). Comparing the conformations of  $\beta$ -catenin in ABE and in V(T12K3E) indicates that the long and disordered N-terminal region of β-catenin is more extended within the V(T12K3E)ABE than in the ABE complex (Fig. 4 D and E).

EOM analysis of the SANS data indicates that  $\beta$ -catenin in the ABE complex has a broad conformational distribution with  $R_{\rm g}$  between 40 and 60 Å and  $D_{\rm max}$  between 130 and 260 Å (Fig. S12 B, black data). However, the conformation β-catenin in the V(T12K3E)ABE complex displays two distinct populations. One population of 55.4% is more compact with R<sub>g</sub> peaks at 43.6 Å and D<sub>max</sub> peaks at 137.4 Å. The other population of 44.6% is more extended with  $R_{\tt g}$  between 60 and 76 Å and  $D_{max}$  between 210 and 270 Å (Fig. S12 B, red data). The distinct conformation distribution of β-catenin in the V(T12K3E)ABE complex is due to the long and disordered N-terminal tail in β-catenin as revealed by the EOM-selected structures (Fig. S12 C). Because of the spatial proximity of the N-terminal disordered segment of β-catenin with the Vh domain in the V(T12K3E)ABE complex (see below), it is likely the extended N-terminal disordered population of β-catenin interacts with the Vh domain in the V(T12K3E)ABE complex.

# An ensemble of highly flexible VABE conformations employs vinculin for F-actin binding

The conformation of the deuterated <sup>d</sup>A<sup>d</sup>B<sup>d</sup>E in complex to hydrogenated V(T12K3E) was measured by SANS in 42%  $D_2O$  (Figs. 5 A-G and S13 A-C). The results show that,

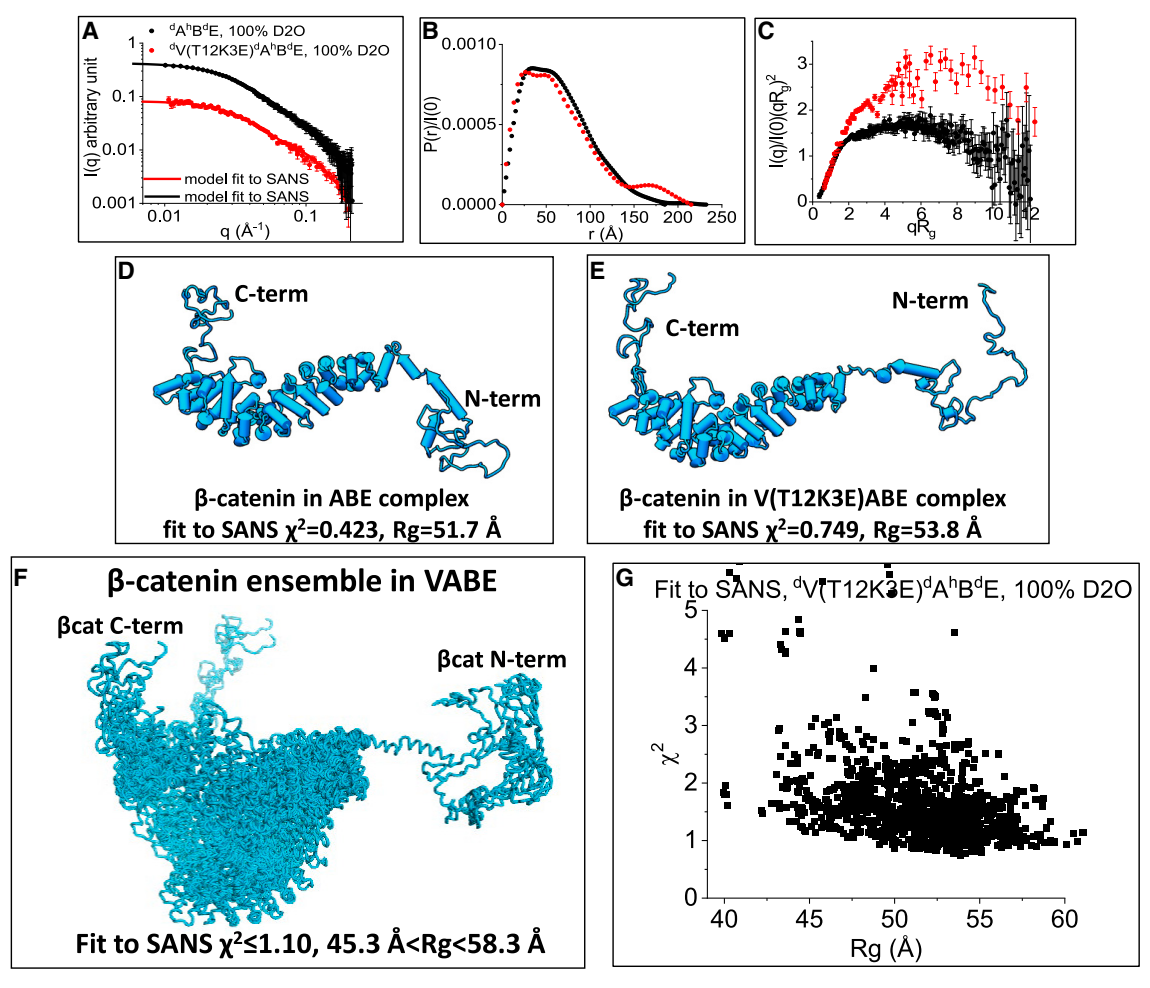


FIGURE 4 β-Catenin conformation in ABE and in VABE. (A) SANS of β-catenin in <sup>d</sup>A<sup>h</sup>B<sup>d</sup>E in 100% D<sub>2</sub>O (black) from (33) and in <sup>d</sup>V(T12K3E)<sup>d</sup>A<sup>h</sup>B<sup>d</sup>E in 100% D2O (red). The lines are the best fit of the theoretical curves computed from the Monte Carlo simulation-generated structures that are selected by SANS data. Guinier plots are shown in Fig. S11 A. (B) P(r) function, symbol colors are the same as in (A). Quality of P(r) fit is shown in Fig. S11 B. (C) Normalized Kratky plots, symbol colors are the same as (A). (D) One representative structural model of β-catenin in ABE from the ensemble of simulation-generated structures that are selected against SANS data of  ${}^dA^hB^dE$  100%  $D_2O$  complex. The shown structure has  $R_g = 51.7$  Å and lowest fitting  $\chi^2 = 0.423$  to the SANS data; data taken from (33). (E) One representative structural model of β-catenin in the V(T12K3E)ABE complex from the ensemble of simulationgenerated structures that are selected against SANS data of  $^dV(T12K3E)^dA^hB^hE$  100%  $D_2O$ . The shown structure has  $R_g=51.6$  Å and lowest fitting  $\chi^2=$ 0.749. (F) Ensemble of β-catenin conformations in V(T12K3E)ABE complex obtained by selecting against SANS data of <sup>d</sup>V(T12K3E)<sup>d</sup>A<sup>h</sup>B<sup>d</sup>E in 100%  $D_2O$ , with the  $\chi^2$  selection criteria and ensemble  $R_g$  values specified. (G)  $\chi^2$  versus  $R_g$  plot of fitting Monte Carlo simulation-generated  $\beta$ -catenin structures against SANS data of  ${}^{d}V(T12K3E){}^{d}A^{h}B^{d}E$  in 100% D<sub>2</sub>O.  $\chi^{2}$  versus R<sub>g</sub> plot of  $\beta$ -catenin in ABE complex is shown in Fig. S11 C.

upon binding to V(T12K3E), the conformation of ABE changes considerably compared with ABE alone in solution (Fig. 5A-C). P(r) shows that the size and shape of ABE have changed when ABE is bound to V(T12K3E) with R<sub>g</sub> increased from 69.3  $\pm$  2.8 to 89.9  $\pm$  2.6 Å, and  $D_{max}$ changed from 260 to 352 Å (Fig. 5 B; Table 1). The normalized Kratky plot suggests that ABE becomes more open and more flexible in the V(T12K3E)ABE complex than ABE alone in solution (Fig. 5 C).

For Monte Carlo simulations of the VABE complex, the contrast-matching SANS selected conformations of the full-length  $\alpha$ -catenin from Fig. 3 F and full-length  $\beta$ -catenin from Fig. 4 E were redocked together to form the  $\alpha$ -catenin/ β-catenin complex, using as templates the crystal structures of the binary complexes of  $\alpha$ -catenin N domain bound to the  $\beta$ -catenin N-terminal peptide (PDB: 1dow) (52) and the β-catenin armadillo domain bound to the cytoplasmic tail of E-cadherin (PDB: 1I7X) (51). The open full-length vinculin from Fig. 2 F was redocked to the VBS of  $\alpha$ -catenin in the ABE complex using the crystal structure of the vinculin D1 subdomain in complexed to the VBS peptide of α-catenin (PDB: 4EHP). Monte Carlo simulations were performed on the VABE complexes, assuming flexible linkers in  $\alpha$ -catenin,  $\beta$ -catenin, and vinculin; see supporting experimental procedures for details of VABE complex Monte Carlo simulations and structure selection.

Fitting the pool of Monte Carlo simulation-generated structure pool against the SANS data of <sup>h</sup>V(T12K3E)<sup>d</sup>A<sup>d</sup>B<sup>d</sup>E

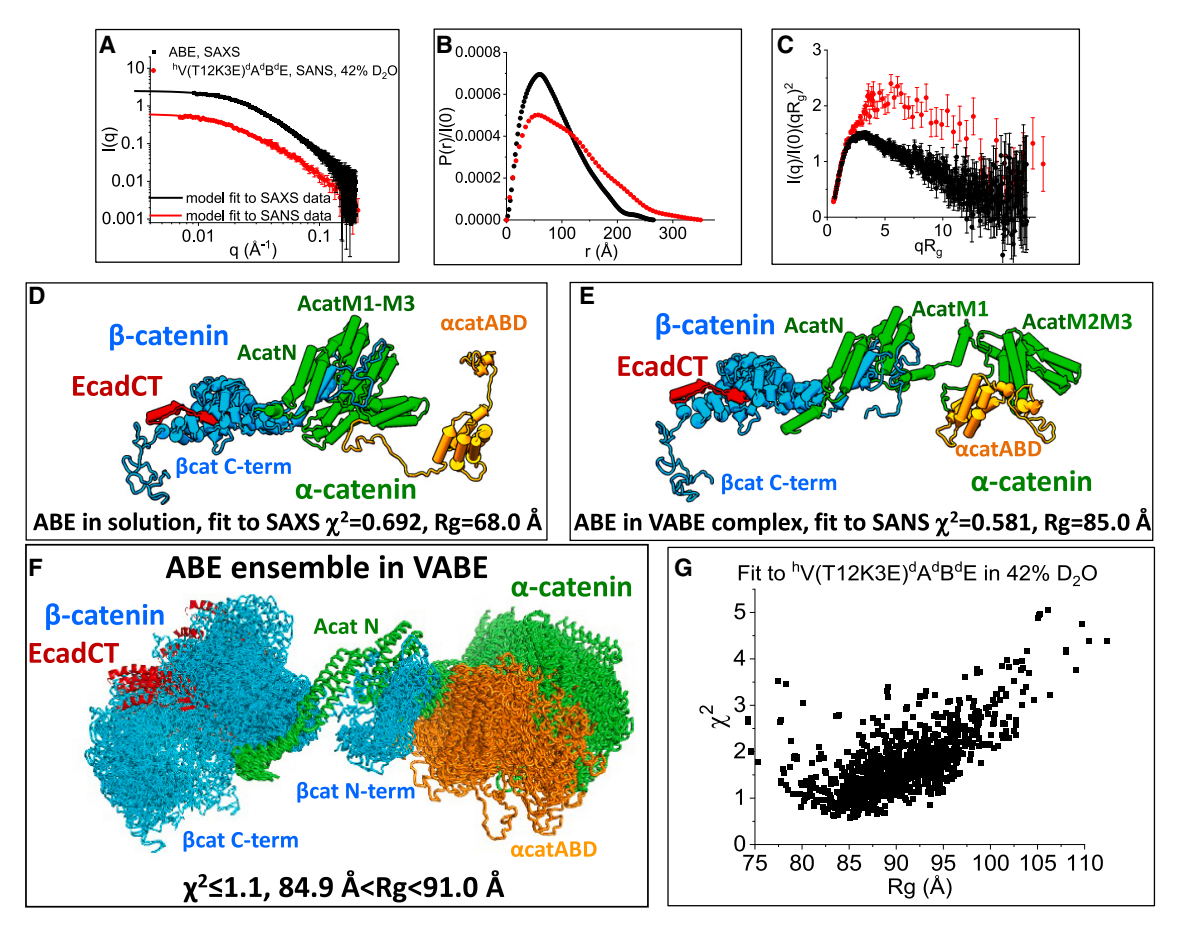


FIGURE 5 Conformation of ABE in solution and in complex with V(T12K3E). (A) SEC-SAXS data of ABE in solution (black), and SANS of <sup>h</sup>V(T12K3E)<sup>d</sup>A<sup>d</sup>B<sup>d</sup>E in 42% D<sub>2</sub>O (red). The lines are the best fit of the theoretical curves computed from the Monte Carlo simulation-generated structures that are selected against the SANS data. Guinier plots are shown in Fig. S13 A. (B) P(r) functions of ABE in solution (black) and in complex with V(T12K3E) (red). Quality of P(r) fit is shown in Fig. S13 B. (C) Normalized Kratky plots, symbol colors are the same as in (A and B). (D) One representative structural model of ABE complex in solution from the ensemble of simulation-generated structures that are against SAXS data of ABE. The shown structure has R<sub>o</sub> = 68.0 Å and lowest fitting  $\chi^2 = 0.692$ . (E) One representative structural model of ABE in the V(T12K3E)ABE complex from the ensemble of simulationgenerated structures that are selected against SANS data of  ${}^{\rm h}V({\rm T}12{\rm K}3{\rm E}){}^{\rm d}A{}^{\rm d}B{}^{\rm d}{\rm E}$  in 42% D<sub>2</sub>O. The shown structure has R<sub>g</sub> = 85.0 Å and lowest fitting  $\chi^2$  = 0.581. (F) Ensemble of Monte Carlo ABE conformations selected by fitting simulation-generated structure pool against SANS data of hV(T12K3E)dAdBdE in 42%  $D_2O$ , with ensemble  $\chi^2$  and  $R_g$  values shown. (G)  $\chi^2$  versus  $R_g$  plot of fitting Monte Carlo simulation generate ABE structures against SANS data of  $^{\rm h}$ V(T12K3E) $^{\rm d}$ A $^{\rm d}$ B $^{\rm d}$ E in 42% D<sub>2</sub>O.  $\chi^2$  versus R<sub>g</sub> plot of ABE in solution is shown in Fig. S13 C.

in 42% D<sub>2</sub>O buffer yields an ensemble of ABE structures in the V(T12K3E)ABE complex (Fig. 5 F and G) with  $\gamma^2 \le$ 1.1. One representative ABE structure in the ensemble is shown in Fig. 5 E, along with the SANS-derived structure of ABE in solution alone obtained from (33) (Fig. 5 D).

Fitting the pool of Monte Carlo-generated structures against the experimental SANS data of hV(T12K3E)dAdBdE in 0% D<sub>2</sub>O in which both the deuterated <sup>d</sup>A<sup>d</sup>B<sup>d</sup>E and hydrogenated V(T12K3E) contribute to the measured scattering or to the SAXS data of V(T12K3E)ABE (Fig. 6 A-D). Fig. 6 E shows one representative VABE structure with the best fit to the SANS data. Fig. 6 F shows the ensemble of VABE structures selected against the SANS data with  $\chi^2$  and  $R_g$  of the ensemble specified in the figure. The VABE complex ensemble is highly flexible, with  $\alpha$ -catenin and  $\beta$ -catenin sampling multiple conformations. Although V(T12K3E) can sample a variety of orientations in the complex ensemble, the conformations of V(T12K3E) are open and extended with VtABD well separated from the Vh domain that is anchored to  $\alpha$ -catenin in the complex (Fig. 6 *E* and *F*).

While acatABD is dynamic having different orientations in the VABE complex, acatABD tends to be in proximity to M2M3 of α-catenin as well as to the Vh domain of vinculin (Figs. 5 E, F, 6 E, and F). This observation led us to speculate that the acatABD may interact with Vh in the VABE complex, which contributes to further impeding the acatABD from binding to F-actin. Using SPR, we determined the binding affinity of Vh (aa 1-840) to acatABD (aa 640-906) with a dissociation constant of  $K_d = 23.5 \pm 2.5 \mu M$  (Fig. S14 A and B). Previous studies reported that the affinity of Vh for VtABD binding has  $K_d = 20-50$  nM (34,74). Although the affinity of Vh for acatABD is much lower than for VtABD, Vh is likely to

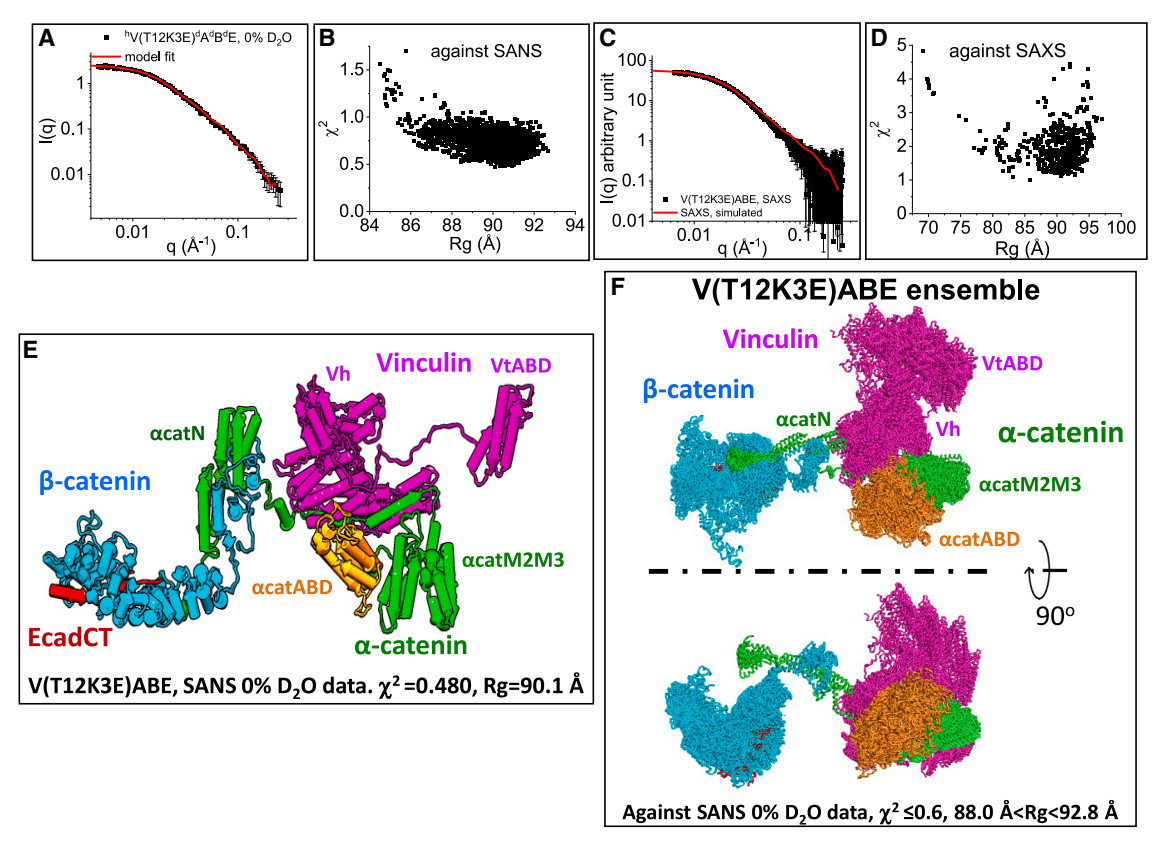


FIGURE 6 Composite VABE conformations selected against SAXS and SANS. (A and B) Model fit (red line) to SANS data of hV(T12K3E)<sup>d</sup>A<sup>d</sup>B<sup>d</sup>E in 0% D2O (black squares). (C and D) Model fit (red line) to SEC-SAXS data of V(T12K3E)ABE complex (black squares). (E) One representative VABE structural model from the ensemble of simulation-generated structures that are selected against SANS data with  $\chi^2$  and  $R_g$  values shown. (F) The ensemble of VABE conformations selected against SANS data  ${}^hV(T12K3E)^dA^dB^dE$  in 0%  $D_2O$  with ensemble  $\chi^2$  and  $R_g$  values shown.

be capable of interacting with acatABD within the VABE complex. This is because VtABD is separated away from Vh by the relatively rigid poly-proline linker in the VABE complex, while acatABD is sterically close to the Vh domain than VtABD. Nevertheless, the interaction between Vh and acatABD is dynamic because, in some of the SANS-selected models, acatABD is well separated away from Vh due to the movement of M2M3-acatABD and  $\alpha$ catABD (Fig. 6 F).

We performed sedimentation assays to determine how the VABE complex binds to F-actin. For F-actin binding experiments, we generated a salt bridge disrupting the vinculin mutant of E14K/E28K/E29K, named V(E3K), and reconstituted the V(E3K)ABE complex (Fig. S3 E and F). Because the V(E3K) mutant has all mutations only in the Vh D1 subdomain in the full-length vinculin, the F-actin binding properties of VtABD are not perturbed by the salt-bridgedisrupting mutations. Notably, previous studies suggest that E28 and E29 in Vh, in particular E29, may prime vinculin for binding to F-actin (75–77).

Sedimentation F-actin binding results are shown in Fig. S15 A-C. SDS-PAGE band intensity analysis shows that only 16.2% of ABE binds to F-actin in the sedimentation pellet, but 83.8% of ABE remains in the supernatant without binding to F-actin (Fig. S15 A, lanes 8–9, and S15 B, table). This result is consistent with previous findings that ABE does not bind F-actin effectively (78). However, V(E3K)ABE binds F-actin, with 88.8% V(E3K)ABE cosedimented with F-actin in the pellet, while 11.2% of V(E3K) ABE is left in the supernatant without binding to F-actin (Fig. S15 A, lanes 5 and 6, and S15 B). In addition, upon adding the V(E3K)ABE complex to F-actin, we observed cloudy precipitations that are likely due to the F-actin bundling function of vinculin (Fig. S15 C). Previous studies reported that vinculin bundles the F-actin microfilaments (79,80).

We then reconstituted two control VABE complexes, one complex with the acatABD removed (named the VA<sub>640</sub>BE-ΔαcatABD complex), and the other complex with the VtABD removed (the Vh<sub>718</sub>ABE-ΔVtABD complex). Sedimentation experiments show that VA<sub>640</sub>BE-ΔαcatABD binds to F-actin completely (Fig. S15 A, lanes 13 and 14). However, only a minor fraction of 13.6% Vh<sub>718</sub>ABE-ΔVtABD binds F-actin in the pellet but a majority of 86.4% Vh<sub>718</sub>ABE-ΔVtABD remains in the supernatant without binding to F-actin (Fig. S15 A, lanes 2 and 3, and S15 B). Together, the F-acting binding results show that the VABE complex employs vinculin as the dominant

F-actin binding factor, and that vinculin as part of VABE bundles F-actin.

#### DISCUSSION

The highly flexible and dynamic conformations of multiprotein complexes pose a significant challenge for structural studies. Here, we adopted a hybrid approach to determine the structure of the VABE complex by combining SAXS and SANS experiments with Monte Carlo simulations. By using the available high-resolution crystal structures of fragments of binary complexes of Vh/ $\alpha$ -catenin VBS, and  $\alpha$ -catenin/β-catenin as docking templates, we first generated a preliminary structural model of the full-length VABE complex. Monte Carlo simulations were then performed on the docked structure to generate a pool of conformations of flexible  $\alpha$ -catenin,  $\beta$ -catenin, and vinculin as parts of the VABE complex. SANS data at different contrast-matching points were then used as constraints to select the conformation ensemble  $\alpha$ -catenin,  $\beta$ -catenin, vinculin, ABE, and the whole VABE complex. With this hybrid approach, we provide all-atomic models of the ensemble of the full-length vinculin, α-catenin, and β-catenin in the VABE complex as well as the whole VABE complex.

The major finding from this study is that ionic interactions at the interface between the vinculin Vh and Vt domains are the primary factor that locks vinculin in the autoinhibited conformation. By disrupting the ionic interactions, we were able to reconstitute the cadherin-catenin-vinculin VABE complex. In the reconstituted VABE complex, vinculin adopts an ensemble of extended open conformation with the VtABD well separated from the Vh domain. The whole VABE complex and the vinculin within the VABE complex bind F-actin robustly and bundle F-actin. However, only a minor fraction of α-catenin binds F-actin in the VABE complex, which is the same as the F-actin binding behavior of the ABE complex [78]. Thus, upon recruiting vinculin, the cadherin-catenin complex switches to employ vinculin as the primary F-actin binding mode, and bundles the F-actin microfilaments as depicted in Fig.7.

The distribution and composition of AJs are heterogeneous in cell-cell adhesion (1,81,82). During dynamic tissue remodeling, AJs likely employ different F-actin binding modes to adapt to different mechanical requirements. In quiescent tissues, the dynamic cadherin-catenin F-actin binding mode may enable the cadherin-catenin complexes to slide along the actin microfilaments. However, when strong mechanical couplings between the neighboring cell membrane-cytoskeleton are required, such as during collective cell migration in morphogenesis, the AJs recruit vinculin to the cadherin-catenin complex and switch to the vinculin F-actin binding mode that bundles the actin microfilament (23,83). There is also the redundancy in the cadherin-catenin-vinculin complex: ABE can still bind albeit less effectively. In addition, our results provide a structural explanation to previous cell biological and biochemical findings that vinculin is necessary for the maintenance of epithelial AJs, but cells lacking α-catenin ABD are able to form AJs (84).

Our experiments show that the binding of the ABE complex to the active full-length vinculin does not require mechanical force. This result agrees with biochemical findings

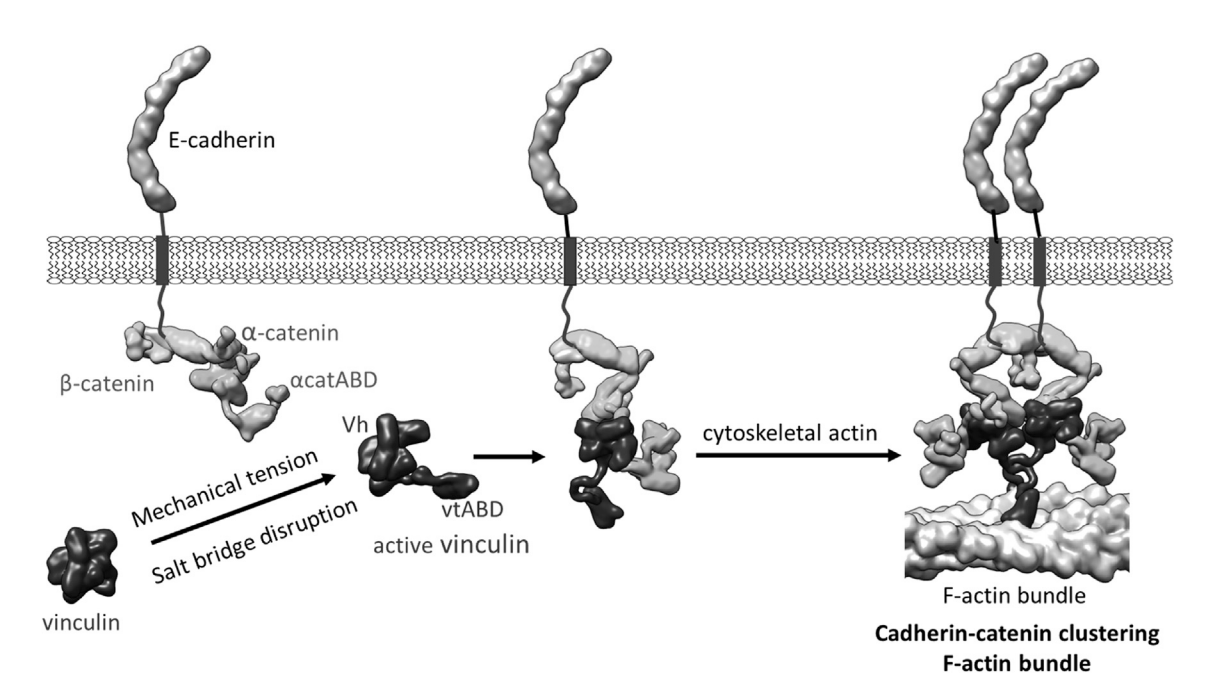


FIGURE 7 A cartoon depicting the activated vinculin that binds to the cadherin-catenin complex. The cartoon also shows the hypothetical dimerization of the VABE complex upon binding to F-actin, and the bundling of two actin micro-filaments by two cadherin-catenin-vinculin complexes.

Shi et al.

that Vh forms a complex with  $\alpha E$ -catenin or with αT-catenin through incubation without the need to apply mechanical tension in  $\alpha$ -catenin (46,85,86). However, single-molecule magnetic tweezer experiments showed that mechanical forces are required to unfold the M domain of  $\alpha E$ -catenin to expose the VBS in M1 for vinculin binding (48). The discrepancy of observations about whether mechanical tension is required for the binding of vinculin to α-catenin from different types of experiments may be explained by the dynamic interaction of M1 with the M2-M3 subdomains in α-catenin. Studies have shown that  $\alpha E$ -catenin has fewer masking interactions between the M1 and M2-M3 subdomains than  $\alpha$ N-catenin (87), and that the M1 subdomain of  $\alpha E$ -catenin is dynamic within the M domain (47). The dynamic motion in the M domain may expose the VBS of  $\alpha E$ -catenin M1 in open states that are capable of binding to vinculin without the need for mechanical force. The presence of active vinculin shifts the population of M1 in open states. The  $\sim$ 5 pN magnitude of applied force employed in the magnetic tweezer study (48) likely accelerates the kinetics process of such conformation shift of M1 to open state for binding to Vh. However, the activation of vinculin requires larger mechanical tension of about 40 pN (41) than that required to unmask M1 from the M2M3 subdomains in  $\alpha$ -catenin. Thus, in cells under mechanical tension, the disruption of vinculin autoinhibition is likely to be the limiting factor that regulates the recruitment of vinculin to the AJs because the opening of vinculin requires stronger mechanical force than unmasking M1 from M2M3 domains of α-catenin.

The analysis of the conformation of  $\beta$ -catenin in the V(T12K3E)ABE complex by EOM reveals a bimodal R<sub>g</sub> distribution with peaks near 45 and 65 Å (Fig. S12). Nevertheless, Monte Carlo analysis using the SASSIE package shows a narrower conformation distribution with R<sub>g</sub> from 45 to 58 Å (Fig. 4 F). The discrepancy is likely due to the different conformation sampling processes employed by the different programs. Further studies are needed to employ an independent computational approach to verify the different views generated by SASSIE and EOM.

This study focuses on determining the structure of fulllength vinculin in complex with the cytoplasmic cadherin-catenin complex. Recent cell biophysical studies demonstrate that vinculin influences the E-cadherin extracellular domain assembly and rigidity sensing (88). The vinculin-associated AJs are also known to form nanoscale clusters in cells (89). It remains to be determined about how catenin and vinculin binding affects the conformation of full-length cadherin across the cell membrane, and how the cadherin-catenin-vinculin complex clusters and bundles the actin filaments to provide structural mechanisms by which the vinculin-associated AJs transduce mechanical signals in the membrane-cytoskeleton in cell-cell adhesion.

#### SUPPORTING MATERIAL

Supporting material can be found online at https://doi.org/10.1016/j.bpj. 2023.04.026.

#### **AUTHOR CONTRIBUTIONS**

Conceptualization, I.D.N., D.J.E.C., and Z.B.; methodology, B.S., T.M., S.Q., T.M.W., D.J.E.C., and Z.B.; investigation, B.S., T.M., S.Q., T.M.W., I.D.N., D.J.E.C., and Z.B.; writing, Z.B., T.M., S.Q., T.M.W., I.D.N., and D.J.E.C.; supervision, Z.B.

#### **ACKNOWLEDGMENTS**

This research was funded by NSF grants MCB-1817684 and MCB-2202202 to Z.B. B.S. was supported by a G-RISE Ph.D. traineeship from the National Institutes of Health (grant no. T32GM136499). We would like to acknowledge the Imaging Facility of Advanced Science Research Center at the CUNY Graduate Center for instrument use, scientific and technical assistance, and to thank Dr. Tong Wang for helpful discussions of the negative stain EM results.

Some of this work was performed at the Simons Electron Microscopy Center at the New York Structural Biology Center (NYSBC), with major support from the Simons Foundation (SF349247). We thank the staff members at the NYSBC for training the graduate student. Use of the Stanford Synchrotron Radiation Lightsource (SSRL), SLAC National Accelerator Laboratory, is supported by the U.S. Department of Energy, Office of Science, Office of Basic Energy Sciences under contract no. DE-AC02-76SF00515. The SSRL Structural Molecular Biology Program is supported by the DOE Office of Biological and Environmental Research, and by the National Institutes of Health, National Institute of General Medical Sciences (P30GM133894). The contents of this publication are solely the responsibility of the authors and do not necessarily represent the official views of NIGMS or NIH. The Pilatus detector at Beamline 4-2 at SSRL was funded under National Institutes of Health grant S10OD021512. This research used resources at the High Flux Isotope Reactor, a Department of Energy Office of Science User Facility operated by the Oak Ridge National Laboratory.

#### **DECLARATION OF INTERESTS**

The authors declare no competing interests.

## **REFERENCES**

- 1. Takeichi, M. 2014. Dynamic contacts: rearranging adherens junctions to drive epithelial remodelling. Nat. Rev. Mol. Cell Biol. 15:397-410. https://doi.org/10.1038/nrm3802.
- 2. Shapiro, L., and W. I. Weis. 2009. Structure and biochemistry of cadherins and catenins. Cold Spring Harb. Perspect. Biol. 1:a003053. https://doi.org/10.1101/cshperspect.a003053.
- 3. Angulo-Urarte, A., T. van der Wal, and S. Huveneers. 2020. Cell-cell junctions as sensors and transducers of mechanical forces. Biochim. Biophys. Acta. Biomembr. 1862, 183316.
- 4. Mendonsa, A. M., T. Y. Na, and B. M. Gumbiner. 2018. E-cadherin in contact inhibition and cancer. Oncogene. 37:4769-4780. https://doi. org/10.1038/s41388-018-0304-2.
- 5. Thiery, J. P. 2002. Epithelial-mesenchymal transitions in tumour progression. Nat. Rev. Cancer. 2:442-454. https://doi.org/10.1038/nrc822.
- 6. Mayor, R., and S. Etienne-Manneville. 2016. The front and rear of collective cell migration. Nat. Rev. Mol. Cell Biol. 17:97-109. https://doi. org/10.1038/nrm.2015.14.

- 7. Brasch, J., O. J. Harrison, ..., L. Shapiro. 2012. Thinking outside the cell: how cadherins drive adhesion. Trends Cell Biol. 22:299-310. https://doi.org/10.1016/j.tcb.2012.03.004.
- 8. Borghi, N., M. Sorokina, ..., A. R. Dunn. 2012. E-cadherin is under constitutive actomyosin-generated tension that is increased at cellcell contacts upon externally applied stretch. Proc. Natl. Acad. Sci. USA. 109:12568–12573. https://doi.org/10.1073/pnas.1204390109.
- 9. Yonemura, S., Y. Wada, ..., M. Shibata. 2010. alpha-Catenin as a tension transducer that induces adherens junction development. Nat. Cell Biol. 12:533–542. https://doi.org/10.1038/ncb2055.
- 10. Buckley, C. D., J. Tan, ..., A. R. Dunn. 2014. Cell adhesion. The minimal cadherin-catenin complex binds to actin filaments under force. Science. 346, 1254211. https://doi.org/10.1126/science.1254211.
- 11. Murrell, M., P. W. Oakes, ..., M. L. Gardel. 2015. Forcing cells into shape: the mechanics of actomyosin contractility. Nat. Rev. Mol. Cell Biol. 16:486-498. https://doi.org/10.1038/nrm4012.
- 12. Mège, R. M., and N. Ishiyama. 2017. Integration of cadherin adhesion and cytoskeleton at adherens junctions. Cold Spring Harb. Perspect. Biol. 9, a028738. https://doi.org/10.1101/cshperspect.a028738.
- 13. Cai, D., S. C. Chen, ..., D. J. Montell. 2014. Mechanical feedback through E-cadherin promotes direction sensing during collective cell migration. Cell. 157:1146-1159. https://doi.org/10.1016/j.cell.2014. 03.045.
- 14. Pinheiro, D., and Y. Bellaïche. 2018. Mechanical force-driven adherens junction remodeling and epithelial dynamics. Dev. Cell. 47:3-19. https://doi.org/10.1016/j.devcel.2018.09.014.
- 15. Huveneers, S., and J. de Rooij. 2013. Mechanosensitive systems at the cadherin-F-actin interface. J. Cell Sci. 126 (Pt 2):403-413. https://doi. org/10.1242/jcs.109447.
- 16. Leckband, D. E., and J. de Rooij. 2014. Cadherin adhesion and mechanotransduction. Annu. Rev. Cell Dev. Biol. 30:291-315. https://doi.org/ 10.1146/annurev-cellbio-100913-013212
- 17. Ishiyama, N., S. H. Lee, ..., M. Ikura. 2010. Dynamic and static interactions between p120 catenin and E-cadherin regulate the stability of cell-cell adhesion. Cell. 141:117-128. https://doi.org/10.1016/j.cell.
- 18. Bertocchi, C., Y. Wang, ..., P. Kanchanawong. 2017. Nanoscale architecture of cadherin-based cell adhesions. Nat. Cell Biol. 19:28-37. https://doi.org/10.1038/ncb3456.
- 19. Carvalho, J. R., I. C. Fortunato, ..., C. A. Franco. 2019. Non-canonical Wnt signaling regulates junctional mechanocoupling during angiogenic collective cell migration. Elife. 8, e45853. https://doi.org/10. 7554/eLife.45853.
- 20. Friedl, P., and D. Gilmour. 2009. Collective cell migration in morphogenesis, regeneration and cancer. Nat. Rev. Mol. Cell Biol. 10:445-457. https://doi.org/10.1038/nrm2720.
- 21. Merkel, C. D., Y. Li, ..., A. V. Kwiatkowski. 2019. Vinculin anchors contractile actin to the cardiomyocyte adherens junction. Mol. Biol. Cell. 30:2639–2650. https://doi.org/10.1091/mbc.E19-04-0216.
- 22. le Duc, Q., Q. Shi, ..., J. de Rooij. 2010. Vinculin potentiates E-cadherin mechanosensing and is recruited to actin-anchored sites within adherens junctions in a myosin II-dependent manner. J. Cell Biol. 189:1107–1115. https://doi.org/10.1083/jcb.201001149.
- 23. Huveneers, S., J. Oldenburg, ..., J. de Rooij. 2012. Vinculin associates with endothelial VE-cadherin junctions to control force-dependent remodeling. J. Cell Biol. 196:641-652. https://doi.org/10.1083/jcb.
- 24. Seddiki, R., G. H. N. S. Narayana, ..., R. M. Mège. 2018. Force-dependent binding of vinculin to α-catenin regulates cell-cell contact stability and collective cell behavior. Mol. Biol. Cell. 29:380-388.
- 25. Zemljic-Harpf, A. E., J. C. Miller, ..., R. S. Ross. 2007. Cardiac-myocyte-specific excision of the vinculin gene disrupts cellular junctions, causing sudden death or dilated cardiomyopathy. Mol. Cell Biol. 27:7522-7537. https://doi.org/10.1128/mcb.00728-07.
- 26. Shiraishi, I., D. G. Simpson, ..., T. K. Borg. 1997. Vinculin is an essential component for normal myofibrillar arrangement in fetal mouse car-

- diac myocytes. J. Mol. Cell. Cardiol. 29:2041-2052. https://doi.org/10. 1006/imcc.1997.0438.
- 27. Xu, W., H. Baribault, and E. D. Adamson. 1998. Vinculin knockout results in heart and brain defects during embryonic development. Development. 125:327-337.
- 28. Bays, J. L., and K. A. DeMali. 2017. Vinculin in cell-cell and cell-matrix adhesions. Cell. Mol. Life Sci. 74:2999-3009. https://doi.org/10. 1007/s00018-017-2511-3.
- 29. Grashoff, C., B. D. Hoffman, ..., M. A. Schwartz. 2010. Measuring mechanical tension across vinculin reveals regulation of focal adhesion dynamics. Nature. 466:263-266. https://doi.org/10.1038/nature09198.
- 30. Thompson, P. M., C. E. Tolbert, and S. L. Campbell. 2013. Vinculin and metavinculin: oligomerization and interactions with F-actin. FEBS Lett. 587:1220-1229. https://doi.org/10.1016/j.febslet.2013. 02.042.
- 31. Zaidel-Bar, R., S. Itzkovitz, ..., B. Geiger. 2007. Functional atlas of the integrin adhesome. Nat. Cell Biol. 9:858-867. https://doi.org/10.1038/ ncb0807-858.
- 32. Biswas, R., A. Banerjee, ..., S. Raghavan. 2021. Mechanical instability of adherens junctions overrides intrinsic quiescence of hair follicle stem cells. Dev. Cell. 56:761-780.e7. https://doi.org/10.1016/j.devcel. 2021.02.020.
- 33. Bush, M., B. M. Alhanshali, ..., Z. Bu. 2019. An ensemble of flexible conformations underlies mechanotransduction by the cadherin-catenin adhesion complex. Proc. Natl. Acad. Sci. USA. 116:21545-21555. https://doi.org/10.1073/pnas.1911489116.
- 34. Cohen, D. M., H. Chen, ..., S. W. Craig. 2005. Two distinct head-tail interfaces cooperate to suppress activation of vinculin by talin. J. Biol. Chem. 280:17109-17117. https://doi.org/10.1074/jbc.M414704200.
- 35. Grant, T. D. 2018. Ab initio electron density determination directly from solution scattering data. Nat. Methods. 15:191-193. https://doi. org/10.1038/nmeth.4581.
- 36. Sumner, J., and S. Qian. 2022. DENSS-multiple: a structure reconstruction method using contrast variation of small-angle neutron scattering based on the DENSS algorithm. BBA Adv. 2, 100063.
- 37. Franke, D., and D. I. Svergun. 2009. DAMMIF, a program for rapid abinitio shape determination in small-angle scattering. J. Appl. Crystallogr. 42 (Pt 2):342-346. https://doi.org/10.1107/s0021889809000338.
- 38. Chen, H., D. M. Cohen, ..., S. W. Craig. 2005. Spatial distribution and functional significance of activated vinculin in living cells. J. Cell Biol. 169:459-470. https://doi.org/10.1083/jcb.200410100.
- 39. Ziegler, W. H., R. C. Liddington, and D. R. Critchley. 2006. The structure and regulation of vinculin. Trends Cell Biol. 16:453-460. https:// doi.org/10.1016/j.tcb.2006.07.004.
- 40. Bays, J. L., X. Peng, ..., K. A. DeMali. 2014. Vinculin phosphorylation differentially regulates mechanotransduction at cell-cell and cell-matrix adhesions. J. Cell Biol. 205:251-263. https://doi.org/10.1083/jcb. 201309092.
- 41. Sun, L., J. K. Noel, ..., J. N. Onuchic. 2017. Molecular simulations suggest a force-dependent mechanism of vinculin activation. Biophys. J. 113:1697-1710. https://doi.org/10.1016/j.bpj.2017.08.037.
- 42. Rothenberg, K. E., D. W. Scott, ..., B. D. Hoffman. 2018. Vinculin force-sensitive dynamics at focal adhesions enable effective directed cell migration. Biophys. J. 114:1680-1694. https://doi.org/10.1016/j. bpi.2018.02.019.
- 43. Kim, L. Y., P. M. Thompson, ..., G. M. Alushin. 2016. The structural basis of actin organization by vinculin and metavinculin. J. Mol. Biol. 428:10-25. https://doi.org/10.1016/j.jmb.2015.09.031.
- 44. Krokhotin, A., M. Sarker, ..., N. V. Dokholyan. 2019. Distinct binding modes of vinculin isoforms underlie their functional differences. Structure. 27:1527–1536.e3. https://doi.org/10.1016/j.str.2019.07.013.
- 45. Choi, H. J., S. Pokutta, ..., W. I. Weis. 2012. alphaE-catenin is an autoinhibited molecule that coactivates vinculin. Proc. Natl. Acad. Sci. USA. 109:8576–8581. https://doi.org/10.1073/pnas.1203906109.

Shi et al.

- Rangarajan, E. S., and T. Izard. 2012. The cytoskeletal protein alphacatenin unfurls upon binding to vinculin. *J. Biol. Chem.* 287:18492–18499. https://doi.org/10.1074/jbc.M112.351023.
- Hirano, Y., Y. Amano, ..., T. Hakoshima. 2018. The force-sensing device region of alpha-catenin is an intrinsically disordered segment in the absence of intramolecular stabilization of the autoinhibitory form. Gene Cell. 23:370–385. https://doi.org/10.1111/gtc.12578.
- Yao, M., W. Qiu, ..., J. Yan. 2014. Force-dependent conformational switch of alpha-catenin controls vinculin binding. *Nat. Commun.* 5:4525. https://doi.org/10.1038/ncomms5525.
- Le, S., M. Yu, and J. Yan. 2019. Direct single-molecule quantification reveals unexpectedly high mechanical stability of vinculin-talin/α-catenin linkages. Sci. Adv. 5, eaav2720. https://doi.org/10.1126/sciadv. aav2720.
- Kluger, C., L. Braun, ..., V. Vogel. 2020. Different vinculin binding sites use the same mechanism to regulate directional force transduction. *Biophys. J.* 118:1344–1356.
- Huber, A. H., and W. I. Weis. 2001. The structure of the beta-catenin/E-cadherin complex and the molecular basis of diverse ligand recognition by beta-catenin. *Cell.* 105:391–402.
- Pokutta, S., and W. I. Weis. 2000. Structure of the dimerization and beta-catenin-binding region of alpha-catenin. Mol. Cell. 5:533–543.
- Gama Lima Costa, R., and D. Fushman. 2022. Reweighting methods for elucidation of conformation ensembles of proteins. *Curr. Opin.* Struct. Biol. 77, 102470. https://doi.org/10.1016/j.sbi.2022.102470.
- Bondos, S. E., A. K. Dunker, and V. N. Uversky. 2022. Intrinsically disordered proteins play diverse roles in cell signaling. *Cell Commun.* Signal. 20:20.
- Farago, B., I. D. Nicholl, ..., Z. Bu. 2021. Activated nanoscale actinbinding domain motion in the catenin-cadherin complex revealed by neutron spin echo spectroscopy. *Proc. Natl. Acad. Sci. USA*. 118, e2025012118. https://doi.org/10.1073/pnas.2025012118.
- Nicholl, I. D., T. Matsui, ..., Z. Bu. 2018. Alpha-catenin structure and nanoscale dynamics in solution and in complex with F-actin. *Biophys. J.* 115:642–654. https://doi.org/10.1016/j.bpj.2018.07.005.
- Johnson, R. P., and S. W. Craig. 1994. An intramolecular association between the head and tail domains of vinculin modulates talin binding. *J. Biol. Chem.* 269:12611–12619.
- Chorev, D. S., T. Volberg, ..., B. Geiger. 2018. Conformational states during vinculin unlocking differentially regulate focal adhesion properties. *Sci. Rep.* 8:2693. https://doi.org/10.1038/s41598-018-21006-8.
- Manalastas-Cantos, K., P. V. Konarev, ..., D. Franke. 2021. Atsas 3.0: expanded functionality and new tools for small-angle scattering data analysis. J. Appl. Crystallogr. 54 (Pt 1):343–355. https://doi.org/10. 1107/s1600576720013412.
- 60. Moore, P. B. 1982. Small-angle scattering techniques for the study of biological macromolecules and macromolecular aggregates. *In* Methods in Experimental Physics Elsevier, pp. 337–390.
- Trewhella, J. 2016. Small-angle scattering and 3D structure interpretation. Curr. Opin. Struct. Biol. 40:1–7. https://doi.org/10.1016/j.sbi. 2016.05.003.
- Jayasundar, J. J., J. H. Ju, ..., Z. Bu. 2012. Open conformation of ezrin bound to phosphatidylinositol 4,5-bisphosphate and to F-actin revealed by neutron scattering. *J. Biol. Chem.* 287:37119–37133. https://doi.org/ 10.1074/jbc.M112.380972.
- Johansen, N. T., M. C. Pedersen, ..., L. Arleth. 2018. Introducing SEC-SANS for studies of complex self-organized biological systems. *Acta Crystallogr. D Struct. Biol.* 74 (Pt 12):1178–1191. https://doi.org/10.1107/s2059798318007180.
- **64.** Jacrot, B., and G. Zaccai. 1981. Determination of molecular weight by neutron scattering. *Biopolymers*. 20:2413–2426.
- Li, J., D. J. E. Callaway, and Z. Bu. 2009. Ezrin induces long-range interdomain allostery in the scaffolding protein NHERF1. *J. Mol. Biol.* 392:166–180.

- Tria, G., H. D. T. Mertens, ..., D. I. Svergun. 2015. Advanced ensemble modelling of flexible macromolecules using X-ray solution scattering. *IUCrJ*. 2 (Pt 2):207–217. https://doi.org/10.1107/s205225251500202x.
- Bernadó, P., and D. I. Svergun. 2012. Structural analysis of intrinsically disordered proteins by small-angle X-ray scattering. *Mol. Biosyst*. 8:151–167. https://doi.org/10.1039/c1mb05275f.
- Yang, J., R. Yan, ..., Y. Zhang. 2015. The I-TASSER Suite: protein structure and function prediction. *Nat. Methods*. 12:7–8. https://doi. org/10.1038/nmeth.3213.
- Receveur-Brechot, V., and D. Durand. 2012. How random are intrinsically disordered proteins? A small angle scattering perspective. *Curr. Protein Pept. Sci.* 13 (1):55–75.
- Durand, D., C. Vivès, ..., F. Fieschi. 2010. NADPH oxidase activator p67(phox) behaves in solution as a multidomain protein with semi-flexible linkers. *J. Struct. Biol.* 169:45–53. https://doi.org/10.1016/j.jsb. 2009.08.009.
- Curtis, J. E., S. Raghunandan, ..., S. Krueger. 2012. SASSIE: a program to study intrinsically disordered biological molecules and macromolecular ensembles using experimental scattering restraints. *Comput. Phys. Commun.* 183:382–389.
- Pettersen, E. F., T. D. Goddard, ..., T. E. Ferrin. 2004. UCSF Chimeraa visualization system for exploratory research and analysis. *J. Comput. Chem.* 25:1605–1612.
- Peng, X., L. E. Cuff, ..., K. A. DeMali. 2010. Vinculin regulates cell-surface E-cadherin expression by binding to beta-catenin. *J. Cell Sci.* 123 (Pt 4):567–577. https://doi.org/10.1242/jcs.056432.
- Bakolitsa, C., D. M. Cohen, ..., R. C. Liddington. 2004. Structural basis for vinculin activation at sites of cell adhesion. *Nature*. 430:583–586. https://doi.org/10.1038/nature02610.
- Golji, J., and M. R. K. Mofrad. 2013. The interaction of vinculin with actin. *PLoS Comput. Biol.* 9, e1002995. https://doi.org/10.1371/journal.pcbi.1002995.
- Janssen, M. E. W., E. Kim, ..., D. Hanein. 2006. Three-dimensional structure of vinculin bound to actin filaments. Mol. Cell. 21:271–281.
- 77. Auernheimer, V., and W. H. Goldmann. 2014. Vinculin E29R mutation changes cellular mechanics. *Biochem. Biophys. Res. Commun.* 452:661–664. https://doi.org/10.1016/j.bbrc.2014.08.133.
- Drees, F., S. Pokutta, ..., W. I. Weis. 2005. Alpha-catenin is a molecular switch that binds E-cadherin-beta-catenin and regulates actin-filament assembly. *Cell.* 123:903–915. https://doi.org/10.1016/j.cell.2005.09.021.
- Jockusch, B. M., and G. Isenberg. 1981. Interaction of alpha-actinin and vinculin with actin: opposite effects on filament network formation. *Proc. Natl. Acad. Sci. USA*. 78:3005–3009. https://doi.org/10. 1073/pnas.78.5.3005.
- Shen, K., C. E. Tolbert, ..., S. L. Campbell. 2011. The vinculin C-terminal hairpin mediates F-actin bundle formation, focal adhesion, and cell mechanical properties. *J. Biol. Chem.* 286:45103–45115. https://doi.org/10.1074/jbc.M111.244293.
- Biswas, K. H., K. L. Hartman, ..., J. T. Groves. 2015. E-cadherin junction formation involves an active kinetic nucleation process. *Proc. Natl. Acad. Sci. USA*. 112:10932–10937. https://doi.org/10.1073/pnas.1513775112.
- Wu, Y., P. Kanchanawong, and R. Zaidel-Bar. 2015. Actin-delimited adhesion-independent clustering of E-cadherin forms the nanoscale building blocks of adherens junctions. *Dev. Cell.* 32:139–154. https:// doi.org/10.1016/j.devcel.2014.12.003.
- Thomas, W. A., C. Boscher, ..., S. Dufour. 2013. α-Catenin and vinculin cooperate to promote high E-cadherin-based adhesion strength. J. Biol. Chem. 288:4957–4969. https://doi.org/10.1074/jbc. M112.403774.
- Taguchi, K., T. Ishiuchi, and M. Takeichi. 2011. Mechanosensitive EPLIN-dependent remodeling of adherens junctions regulates epithelial reshaping. J. Cell Biol. 194:643–656. https://doi.org/10.1083/jcb. 201104124.

Dynamic structure of the cadherin-catenin-vinculin complex

- 85. Rangarajan, E. S., and T. Izard. 2013. Dimer asymmetry defines alphacatenin interactions. Nat. Struct. Mol. Biol. 20:188-193. https://doi. org/10.1038/nsmb.2479.
- 86. Heier, J. A., S. Pokutta, ..., A. V. Kwiatkowski. 2021. Distinct intramolecular interactions regulate autoinhibition of vinculin binding in αTcatenin and aE-catenin. J. Biol. Chem. 296, 100582. https://doi.org/ 10.1016/j.jbc.2021.100582.
- 87. Ishiyama, N., N. Tanaka, ..., M. Ikura. 2013. An autoinhibited structure of alpha-catenin and its implications for vinculin recruitment to adherens junctions. J. Biol. Chem. 288:15913–15925. https://doi.org/10. 1074/jbc.M113.453928.
- 88. Yang, Y. A., E. Nguyen, ..., M. P. Sheetz. 2022. Local contractions regulate E-cadherin rigidity sensing. Sci. Adv. 8, eabk0387. https:// doi.org/10.1126/sciadv.abk0387.
- 89. Troyanovsky, R. B., A. P. Sergeeva, ..., S. M. Troyanovsky. 2021. Sorting of cadherin-catenin-associated proteins into individual clusters. Proc. Natl. Acad. Sci. USA. 118, e2105550118. https://doi.org/10. 1073/pnas.2105550118.
- 90. Chen, X., J. A. Khajeh, ..., Z. Bu. 2015. Phosphatidylinositol 4,5-bisphosphate clusters the cell adhesion molecule CD44 and assembles a specific CD44-Ezrin heterocomplex, as revealed by small angle

- neutron scattering. J. Biol. Chem. 290:6639-6652. https://doi.org/10. 1074/jbc.M114.589523.
- 91. Bhattacharya, S., J. H. Ju, ..., Z. Bu. 2013. Ligand-induced dynamic changes in extended PDZ domains from NHERF1. J. Mol. Biol. 425:2509–2528. https://doi.org/10.1016/j.jmb.2013.04.001.
- 92. Callaway, D. J. E., and Z. Bu. 2016. Essential strategies for revealing nanoscale protein dynamics by neutron spin echo spectroscopy. Methods Enzymol. 566:253-270. https://doi.org/10.1016/bs.mie.2015.
- 93. Smolsky, I. L., P. Liu, ..., H. Tsuruta. 2007. Biological small-angle X-ray scattering facility at the Stanford Synchrotron radiation laboratory. J. Appl. Crystallogr. 40:s453-s458.
- 94. Heller, W. T., M. Cuneo, ..., W. Bras. 2018. The suite of small-angle neutron scattering instruments at Oak Ridge National Laboratory. J. Appl. Crystallogr. 51:242-248.
- 95. Semenyuk, A. V., and D. I. Svergun. 1991. Gnom a program Package for small-angle scattering data-processing. J. Appl. Cryst. 24:537–540.
- 96. Abràmoff, M. D., P. J. Magalhães, and S. J. Ram. 2004. Image processing with ImageJ. Biophot. Int. 11:36-43.